Geochemistry Geophysics Geosystems G3

Article
Volume 13, Number 10
12 October 2012
Q10008, doi:10.1029/2012GC004130
ISSN: 1525-2027

Published by AGU and the Geochemical Society

Characterizing the effect of mantle source, subduction input and melting in the Fonualei Spreading Center, Lau Basin: Constraints on the origin of the boninitic signature of the back-arc lavas

S. Escrig
Department of Earth and Planetary Sciences, Harvard University, 20 Oxford Street, Cambridge, Massachusetts 02138, USA

Now at Ecole Polytechnique Federale de Lausanne, CH-1015 Lausanne, Switzerland (escrig@fas.harvard.edu)

A. Bézos
Laboratoire de Planétologie et Géodynamique, Univiversité de Nantes, FR-44322 Nantes, France

C. H. Langmuir
Department of Earth and Planetary Sciences, Harvard University, 20 Oxford Street, Cambridge, Massachusetts 02138, USA

P. J. Michael
Department of Geosciences, University of Tulsa, 800 S. Tucker Drive, Tulsa, Oklahoma 74104, USA

R. Arculus
Research School of Earth Sciences, Australian National University, GPO Box 4, Canberra, ACT 0200, Australia

[1] New major element, trace element and Pb-Sr-Nd isotope data for glasses from the Fonualei Spreading Center (FSC) constrain the genesis of back-arc basin basalts and the origins of boninites. The FSC is an end-member for global back-arc lavas in terms of low $Ti_{8.0}$ and $Na_{8.0}$, and contains lavas with a boninitic signature. Latitudinal variations reveal a correspondence in location between back-arc and adjacent arc volcanism. The locations of spikes in subduction input and positive bathymetric anomalies along the FSC correspond to the projected location of the arc volcanoes, likely reflecting 3-D convective structure of the mantle wedge. Non-mobile trace elements in arc and back-arc lavas reveal an increasing proportion northward of a re-enriched refractory mantle source, which is supported by isotope data. Quantitative modeling constrains the extents of melting, fraction of enriched mantle and subduction input. For the FSC, extents of melting are exceptionally large. We show a general relationship between extent of melting, subduction input and distance from the arc that applies to both the Eastern Lau Spreading Center and the FSC segment closer to the arc. In the center of the FSC where the arc volcanism is captured by the back-arc, exceptionally high subduction input and even greater extents of melting are observed, producing melts with boninitic signature. Boninitic samples require the juxtaposition of high subduction input and refractory mantle, leading to large integrated extents of melting, an occurrence that can be produced by multiple causes.

Components: 15,900 words, 14 figures.

Keywords: back-arc basalt; back-arc basin; boninite; enrichment processes; mantle wedge; subduction component.

Index Terms: 1040 Geochemistry: Radiogenic isotope geochemistry; 1065 Geochemistry: Major and trace element geochemistry; 3060 Marine Geology and Geophysics: Subduction zone processes (1031, 3613, 8170, 8413).

Received 1 March 2012; **Revised** 5 September 2012; **Accepted** 5 September 2012; **Published** 12 October 2012.

Escrig, S., A. Bézos, C. H. Langmuir, P. J. Michael, and R. Arculus (2012), Characterizing the effect of mantle source, subduction input and melting in the Fonualei Spreading Center, Lau Basin: Constraints on the origin of the boninitic signature of the back-arc lavas, *Geochem. Geophys. Geosyst.*, *13*, Q10008, doi:10.1029/2012GC004130.

1. Introduction

[2] Back-arc spreading centers provide an invaluable perspective on the complex processes that take place at convergent margins. This perspective is clear when back-arc spreading centers are compared to the distinct, spatially separated volcanoes of the arc volcanic front, which tend to produce rather differentiated lavas that are compositionally removed from parental melts coming from the mantle wedge. When the arc edifices are submarine, it is difficult to obtain geological constraints, and the inner structure and compositions of the volcanoes are inaccessible. Furthermore, most arc volcanoes occur at a narrow range of distances above the subducting slab, and hence give a limited spatial snapshot of convergent margin processes. Arc volcanoes are also built on pre-existing lithosphere that can have a major impact on the extent of mantle melting as well as the extent of interaction and modification en route from the mantle wedge to the surface.

[3] Back-arcs have these problems to a much lesser extent. Because they are formed in the extensional environment of an ocean ridge, the youngest magmatism is continuously exposed. The extension also means there is no pre-existing lithosphere, as the ridge creates new lithosphere as it spreads. Lavas are generally more mafic than the adjacent volcanic front. The ridge is a continuous feature providing a continuous along strike perspective that is lacking at the volcanic front. And for many back-arc basins, the arc-ridge distance changes progressively along the back-arc spreading center, providing a record of change with distance from the arc that is rarely manifested at volcanic fronts.

[4] The Fonualei Spreading Center in the northern Lau Basin exemplifies these advantages for making use of a back-arc to study the convergent margin system. As pointed out by *Keller et al.* [2008], its southern end is within 20 km of the volcanic front of the Tonga arc, and the distance to the arc increases progressively northward (20 km to 75 km). This provides a natural experiment to explore how compositions change progressively with depth to the slab. Such a comparison is of particular interest in this region because it can be compared to a similar tectonic environment along the Eastern Lau Spreading Center further to the south, where the ridge also lies progressively further above the slab with increasing northward distance. Are there generalities that apply to both environments from which meaningful constraints on convergent margin processes can be obtained?

[5] In this study we present a major element, trace element and isotope study of all existing samples from the Fonualei Spreading Center. *Keller et al.* [2008] carried out an earlier major and trace element study based on samples from an Australian cruise (NOTOVE) to the same region. Here we report data on the samples collected during NOTOVE as well as data from 32 additional sample locations collected during a 2003 cruise on R/V Kilo Moana. The more extensive sample set and inclusion of isotope data permit a more complete interpretation of the petrogenesis of the volcanics from this region. *Keller et al.* [2008] noted that there appears to be no arc volcanic front trenchwards from the Fonualei Spreading Center. They suggested on the basis of their data that there was no difference between the back-arc basalts and compositions from the volcanic front, and no variations in chemical composition with changing depth to the slab, an observation that they explained by the back-arc having "captured" the volcanic front. In this paper, we use a more complete sample and data set to show that there are variations with slab depth, well-defined differences between the arc and back-arc lavas, and intriguing spatial relationships that correspond

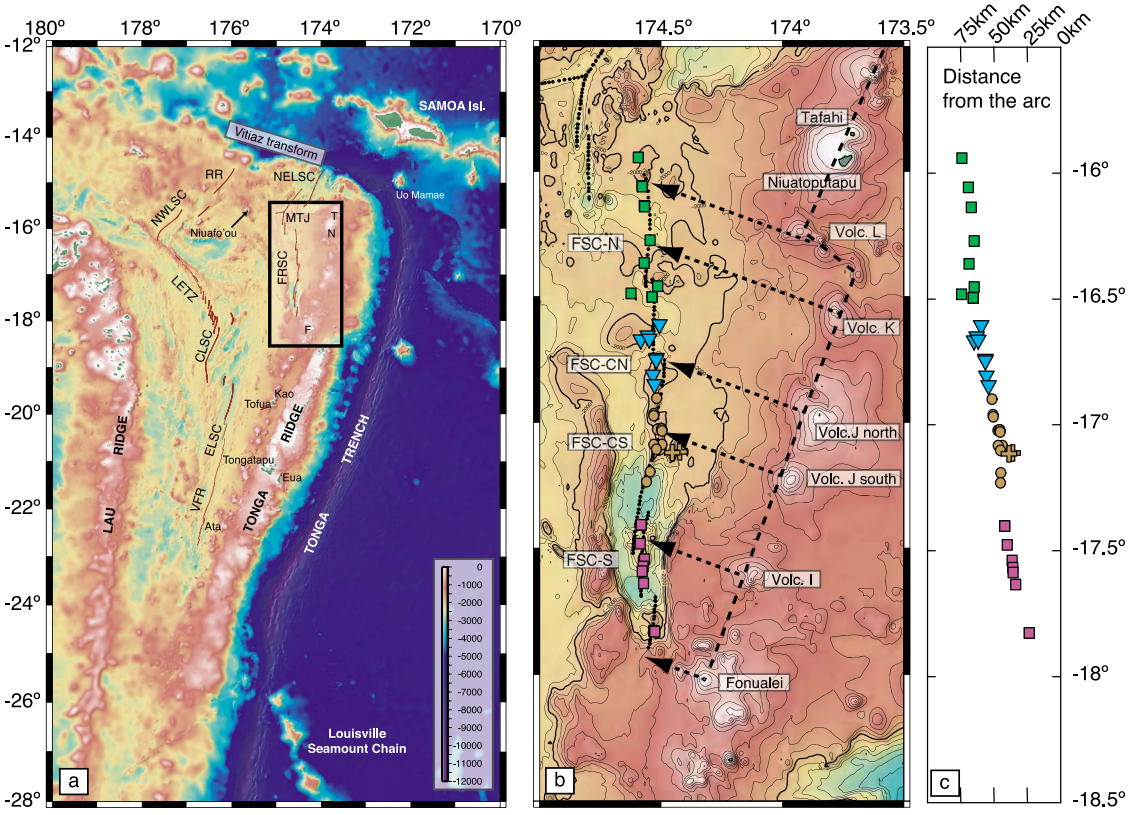

Figure 1. Bathymetric maps of (a) the Lau Basin and (b) the northeast corner of the Lau Basin, with the location and names of the spreading centers. The sample locations are reported using the symbols corresponding to geographical areas defined in the text. (c) The distance from the arc is calculated as the shortest distance from the dashed line going through the Tonga arc volcanoes. Arrows represent the projections of the arc volcanoes perpendicular to the arc front, which correspond to the azimuth given by *Zellmer and Taylor* [2001] (i.e. 109°) for the plate motion.

with the positions of the extinct volcanoes of the volcanic front.

2. Geological Setting and Sample Location

[6] The Lau Basin is a triangular-shaped extensional zone located in the SW Pacific between the Tonga Ridge to the east and the Lau Ridge to the west (Figure 1). The Lau Ridge is a remnant of the paleo-arc, split away by the opening of the back-arc basin at 6 Ma [*Hawkins*, 1995]. The Tonga Ridge is made of two parallel chains of volcanoes, the western chain consisting largely of active subaerial and submarine volcanoes, and a larger eastern ridge that is the other half of the paleoarc and is covered by carbonate platforms [*Hawkins*, 1995]. As the Louisville Seamount Chain is subducted, presently at 24°S, the opening of the Lau Basin gets unlocked and extends southward [*Ruellan et al.*, 2003].

[7] The Lau basin includes numerous spreading centers, usually propagating southward (see Figure 1). Located in the south, the Eastern Lau Spreading Center (ELSC) and its southern extremity the Valu Fa Ridge (VFR) form the longest spreading center of the Lau Basin. It has been the recent focus of geophysical, geochemical, hydrothermal and biological studies as part of the Ridge 2000 program. Just north of the ELSC, a small segment, the ~15 km-long Intermediate Lau Spreading Center (ILSC), makes the transition between the ELSC and the Central Lau Spreading Center (CLSC) which is also mainly oriented N–S. At its northern extremity, the CLSC is made of small 'relay' spreading segments that are extended to the northwest by the Lau Extensional Transform Zone (LETZ). The LETZ joins the Peggy Ridge (PR) that reflects a change of orientation of the spreading as it oriented NW–SE. In the Northeastern part of the Lau basin lies an independent group of spreading centers. Extending

northward from the nearby Fonualei island, the Fonualei Spreading Center (FSC) becomes progressively more distant from the arc front toward the Mangatolu Triple Junction (MTJ). The Mangatolu triple Junction is slightly offset to the West from the FSC, located further away from the arc and closer to the northwest extremity of the Lau Basin. Located between the MTJ and the Fiji fracture zone in the Northeast corner of the Lau Basin lies the Northeast Lau Spreading Center (NE-LSC), with a NE–SW orientation. A few other spreading centers, including the Rochambeau Rifts (RR) and Northwest Lau Spreading Center (NW-LSC) have been identified in the northwestern part of the basin [*Zellmer and Taylor*, 2001].

[8] In this study, we focus on the northeastern corner of the Lau Basin and samples from the active Fonualei Spreading Center (FSC). The Fonualei Spreading Center separates the Tonga Plate and the Niuafo'ou Microplate [*Zellmer and Taylor*, 2001]. Spreading rates increase from 47 mm a-1 in the south to 94 mm a-1 in the north. The spreading centers are elongate volcanic ridges that rise 200–600 m from the floors of rift valleys that are 8–15 km wide and 200–1200 m deeper than surrounding rifted crust. The ridges are 10–20 km long, with left-stepping en echelon offsets that enhance the northward increase in the arc-back-arc offset. There are numerous cones along the ridges, especially in the south, that sometimes rise >1000 m above the valley floors. The valley floors lie at 3000 m in the south and step up to 2400 m deep at around 17°05′S.

[9] This area is particularly interesting for several reasons. First, the distance between the spreading center and the arc front increases progressively toward the north, and the rate of increase with distance is twice as fast as for the ELSC. Comparison between the two spreading centers then provides insights into the relationship between the extent of subduction influence and distance from the trench. Second, the Pacific plate entering the northeastern Lau basin has the fastest total convergence rate of any convergent margin, permitting investigation of the role of convergence rate on back-arc basin geochemistry. Finally, previous investigations of the northern Lau Basin have shown a distinctive isotopic composition (lower Nd and higher Pb and Sr isotope ratios) [*Turner et al.*, 1997; *Ewart et al.*, 1998; *Falloon et al.*, 2007; *Pearce et al.*, 2007; *Falloon et al.*, 2008] and our extensive sample suite permits further elaboration of this geochemical signal and its origin.

[10] Our sample suite consists of 36 locations sampled by rock core and dredge during cruises KM0417 (2004, R/V Kilo Moana) and NoToVe (2004, R/V Southern Surveyor). Station locations and depths are given in Table S1 in the auxiliary material.[1] Some samples from the Surveyor cruise were also analyzed for major and trace element contents by *Keller et al.* [2008]. Most of the samples were collected directly on-axis (see Figure 1b). Only a few samples were collected off axis (ND-42-01 and ND-43-01) located a few km east of the spreading center.

[11] The Fonualei Spreading Center can be divided into 4 sections based on tectonic and geochemical criteria [*Keller et al.*, 2008]: Fonualei Spreading Center South (FSC-S), Fonualei Spreading Center Central South (FSC-CS), Fonualei Spreading Center Central North (FSC-CN), Fonualei Spreading Center North (FSC-N). The sample locations are reported in Figure 1 using the group distinction. Within these groups, the few slightly off-axis samples are distinguished (same color code but different symbol). As shown in the results section, the groups are also clearly distinguishable based on the geochemical data.

3. Analytical Methods

[12] Major element compositions were determined on glassy pillow rims using an electron microprobe (either a JEOL JXA-733 at MIT (KM0417 samples) or a Camebax Micro at the University of Tulsa (NoToVe samples)). All analyses from both labs were normalized to the glass standard VE32 that was run concurrently with samples at regular intervals throughout the analyses, and used as a common standard to ensure no analytical bias between laboratories.

[13] Water contents were analyzed by Fourier Transform Infrared Spectroscopy at the University of Tulsa using a Nicolet 520 FTIR spectrometer equipped with a NicPlan microscope with a HgCdTe detector. For each sample, 4 spot analyses 80 × 80 μm in size were performed on two separate doubly polished wafers, 50–100 mm thick, and averaged. Thicknesses of the wafers were determined using a digital micrometer ($\pm$1 μm precision) and mapped on photographs for reference during analysis. The water concentrations are calculated using the Beer-Lambert law [*Stolper*, 1982; *Dixon et al.*, 1988], for the absorbance at 3535 cm^{-1}. For further

[1]Auxiliary materials are available in the HTML. doi:10.1029/2012GC004130.

details on the analytical method, see *Michael* [1995]. Reproducibility between the replicate analyses was usually less than 7%.

[14] ICP-MS measurements of trace element compositions were performed at Harvard University using a Thermo X-series ICP-MS quadrupole. Fresh glass chips were picked avoiding crystals as much as possible, cleaned and sonicated in de-ionized water. 50 mg were digested overnight in the Picotrace dissolution unit, using 2 mL of 8 N HNO_3 and 0.5 mL of HF at 150°C and then evaporated to dryness. Dried samples were re-dissolved in 4 mL of 4 N HNO_3 and transferred to HDPE bottles with 50 g of Internal Standard solution containing 50 ppb Ge, 25 ppb Rh, 25 ppb In, 25 ppb Tm and 25 ppb Bi and diluted with de-ionized water to 1:5000 of the original sample weight. Raw data were first blank-corrected, then drift-corrected using our in-house standard K1919 (coming from the same lava flow as BHVO-2) and Internal Standards elements. The sample concentrations were calculated using the calibration curves obtained by plotting the drift-corrected values for 5 standards (BHVO-2, W2, DNC-1, JB-2 and another in-house standard MAR) versus their concentrations. Calibration curves typically have a R^2 better than 0.99 and the reproducibility of replicate analyses is generally better than 2% for the REE and elements such as Sc, V, Cr, Rb, Sr, Y, Zr, Nb, Ba and Th, and better than 5% for the others. The standard concentrations for this study are reported in Table S1.

[15] The Pb, Sr, and Nd chemical extractions were performed at Harvard and the isotope ratios determined using a Thermo Neptune MC-ICP-MS at Woods Hole Oceanographic Institution (WHOI). In order to estimate our external reproducibility and ensure that our new data set is comparable with the isotope data obtained on the ELSC lavas, we dissolved and analyzed multiple times the sample KM0417 DR41-1 used by *Escrig et al.* [2009]. Several samples were dissolved and measured twice with a reproducibility consistent with the one obtained for DR41-1.

[16] For Pb analyses, SRM997 (Tl) was used as an internal standard to correct for mass dependent isotopic fractionation. SRM981 (200 ppb Pb solution) was analyzed every few samples and used to normalize the measured values to $^{206}Pb/^{204}Pb$ = 16.9356, $^{207}Pb/^{204}Pb$ = 15.4891, and $^{208}Pb/^{204}Pb$ = 36.7006 [*Todt et al.*, 1996]. 2σ – standard deviation obtained for SRM981 (N = 23) is 122, 130, and 148 ppm, for $^{206}Pb/^{204}Pb$, $^{207}Pb/^{204}Pb$, and $^{208}Pb/^{204}Pb$ ratios, respectively. The average ratios measured for DR41-1 are $^{206}Pb/^{204}Pb$ = 18.270, $^{207}Pb/^{204}Pb$ = 15.506, and $^{208}Pb/^{204}Pb$ = 38.033, with a reproducibility of 49, 156, and 193 ppm (2σ, N = 4), for $^{206}Pb/^{204}Pb$, $^{207}Pb/^{204}Pb$, and $^{208}Pb/^{204}Pb$ ratios, respectively.

[17] Sr isotopic measurements were performed with typical ^{88}Sr beam intensities from 30 to 45 V. $^{87}Sr/^{86}Sr$ ratios were Kr-corrected and normalized to $^{86}Sr/^{88}Sr$ = 0.1194. SRM987 (700 ppb Sr solution) was analyzed every few samples and used to correct the measured sample values to $^{87}Sr/^{86}Sr$ = 0.710235. MC-ICP-MS values for Dr41-1 agree with TIMS data from *Escrig et al.* [2009] within the typical uncertainty. SRM987 measurements average to 0.710236 ± 0.000018 (N = 21). DR41-1 measurements average to 0.703042 ± 0.000025 (2σ, N = 16).

[18] Nd isotopic ratios were measured with typical ^{144}Nd beam intensities from 2 to 3 Volts and normalized to $^{146}Nd/^{144}Nd$ = 0.7219. JNdi (216 ppb solution) was analyzed repeatedly and used to correct the $^{143}Nd/^{144}Nd$ ratios to a value of 0.512115 [*Tanaka et al.*, 2000]. After correction, JNdi average $^{143}Nd/^{144}Nd$ ratio is 0.512115 ± 0.000014 (2σ, N = 21). The average ratio obtained for DR41-1 is 0.513018 ± 0.000012 (2σ, N = 23).

4. Results

[19] Major element contents are reported in Table S1. SiO_2 contents range from 49.2 to 57.5 wt.% and MgO contents from 2.9 to 8.5 wt.%. TiO_2 contents range from 0.4 to 1.1 wt.%, Na_2O from 1.33 to 2.64 wt.% and K_2O from 0.15 to 1 wt.%. Water contents range from 0.72 wt.% up to 1.75 wt.%. The compositions range from basalt to andesite; most of the lavas are basaltic-andesite. A few samples have characteristics approaching boninites as defined by *Crawford et al.* [1989] (SiO_2 > 53 wt.%, TiO_2 < 0.5 wt.%, MgO > 8 wt.%). The low MgO of the FSC samples relative to boninites could be simply explained by the fact that our major element analyses have been performed on glasses avoiding crystals, whereas boninites have been characterized using whole-rock analyses and are known to contain high-Fo olivines [*Crawford et al.*, 1989]. It thus seems that there may be a boninitic signature in the FSC lavas (see below).

[20] The specificity of the FSC lavas is clear when compared with the Eastern Lau Spreading Center samples [*Bézos et al.*, 2009; unpublished data], showing that for most major elements, there is almost no overlap between the two spreading centers

(Figure 2). FSC lavas are distinguished by lower Na_2O, TiO_2 and FeO, and higher K_2O and SiO_2. Al_2O_3 and CaO overlap in part, but at intermediate MgO, the CaO and Al_2O_3 of FSC lavas tend to be higher, reflecting a delayed appearance of plagioclase and clinopyroxene in the FSC lavas, therefore likely higher water contents.

[21] We also report literature data from nearby islands of the Tonga arc, Fonualei (andesites only), Niuatoputapu, and Tafahi [*Turner et al.*, 1997; *Ewart et al.*, 1998; *Hergt and Woodhead*, 2007; *Pearce et al.*, 2007; *Regelous et al.*, 2008; *Turner et al.*, 2012], as well as the island near the southern extremity of the ELSC, Ata. At a given MgO, the FSC data have higher TiO_2 and Na_2O than the neighboring islands, just as the ELSC has higher TiO_2 and Na_2O relative to Ata (Figure 2). Some samples from the FSC have higher K_2O than any of the published island samples.

[22] Comparison of the FSC geographical groups in Figure 2 shows that the groups largely define trends of progressive change with MgO content (and hence temperature) with slopes consistent with liquid lines of descent. These trends confirm the important effect of crystallization on the major element compositions. At the same time, for a few samples within segments, and always between segments, there are distinct offsets in most elements at constant MgO, requiring variations in parental magma compositions. The southerly segments, FSC-S and FSC-CS, have similar FeO, SiO_2 and Na_2O content for a given MgO, but TiO_2 and K_2O contents are lower in the FSC-CS. The FSC-CN has lower TiO_2 and Na_2O and significantly higher SiO_2 compared to the other groups. Finally, the FSC-N has compositions intermediate between the ESLC and the other FSC trends in Na_2O, but has some high TiO_2 but often much higher K_2O.

[23] While there are important differences between the different geographical groups, there is not a single systematic evolution with either the latitude or the distance to the trench. For example, at a given MgO content, the K_2O and TiO_2 contents of the lavas decrease from FSC-S to FSC-CS before increasing in FSC-N. This requires that the variation in primitive melt compositions is not simply related to a single process varying with distance or latitude and has to reflect the combination of multiple processes.

[24] Water content does not covary with MgO content (Figure 2h) but does correlate with depth (Figure S1). Some samples are oversaturated, plotting above the calculated solubility curves [*Dixon et al.*, 1995], indicating that the lavas could not degas fast enough to achieve equilibrium at the eruption depth before quenching. None of our samples have detectable CO_3^{2-}. FTIR detection limits for CO_3^{2-} are quite high because the carbonate absorption peaks at 1515 cm^{-1} and 1435 cm^{-1} are masked by a strong peak for molecular H_2O at 1640 cm^{-1}. Several lines of evidence lead to the conclusion that every sample has degassed some H_2O. First, the FSC samples plot between the solubility curves for 0–35 ppm CO_2, so for more than 35 ppm CO_2, all the samples would be oversaturated and degassed. This contrasts with the fact that, because CO_2 is lost at higher pressure than H_2O [*Dixon et al.*, 1995], its presence would be evidence that H_2O has not been degassed. Second, the positive correlation between H_2O/K_2O and MgO (Figure S2) suggests loss of water loss since the ratio should not change without degassing. Third, most samples are vesicular, and many also contain tiny quench crystals that are symptomatic of H_2O loss.

[25] The trace element compositions of FSC samples (Figure 3) have a strong subduction-like signature with enrichment in fluid-mobile elements (e.g., Cs, Rb, Ba, U, Pb, Sr) and relative depletion in high field strength elements (HFSE), characteristic in some respects of back-arc basalts worldwide [e.g., see *Langmuir et al.*, 2006]. There are important differences, however, between these trace element abundances and the samples in the southern Lau Basin that are closest to the arc, along the Valu Fa ridge. Notably, the heavy rare earth elements (HREE) are lower by almost a factor of two, Nb and Ta are significantly lower, while the "subduction component" trace elements such as Cs, Ba, Th are at about the same levels. The origin of the lower abundances in the FSC lavas compared to the Valu Fa lavas may reflect a higher extent of melting or a more depleted mantle source, as discussed below. In addition to the enrichment in mobile elements, the FSC-N and FSC-CN display less depletion in HFSE (Figure 3b) than the other FSC groups. The comparison with the boninitic depleted and intermediate end-members defined by *Falloon et al.* [2007] (represented by samples 5–24 and 119-2-5, respectively, see *Falloon et al.* [2007] for more details) show that the FSC lavas have highly incompatible element variations that are similar to the depleted boninitic end-member (e.g., with low Th/U) while the flat HREE of the FSC lavas is more similar to the intermediate end-member pattern (sample 119-2-5).

[26] The isotope data show large variations with Pb isotope ratios ranging from 18.503 to 18.775 for $^{206}Pb/^{204}Pb$, from 15.545 to 15.568 for $^{207}Pb/^{204}Pb$,

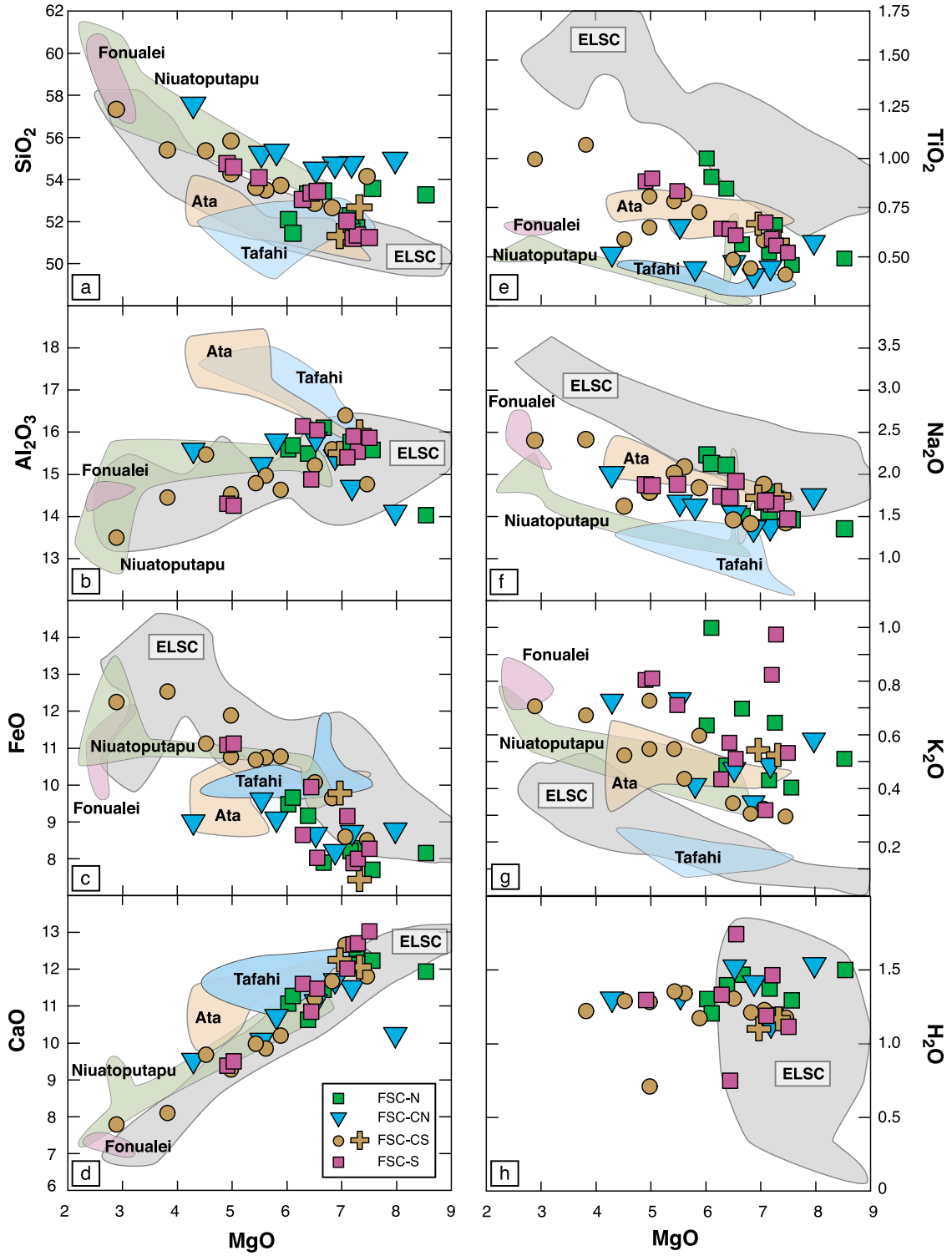

Figure 2. Major element variation diagrams. The data show significant diversity among the FSC groups that do not simply correspond to a regular evolution away from the arc front (e.g., the highest SiO_2 is in FSC-CN in the middle of the study area). Also reported are the fields of the Eastern Lau Spreading Center lavas [*Bézos et al.*, 2009; unpublished data] and relevant Tonga islands (Tafahi, Niuatoputapu and Fonulei's andesites) located near the FSC, and Ata located near the southern ELSC. Data are from *Turner et al.* [1997]; *Ewart et al.* [1998]; *Hergt and Woodhead* [2007]; *Pearce et al.* [2007]; and *Regelous et al.* [2008].

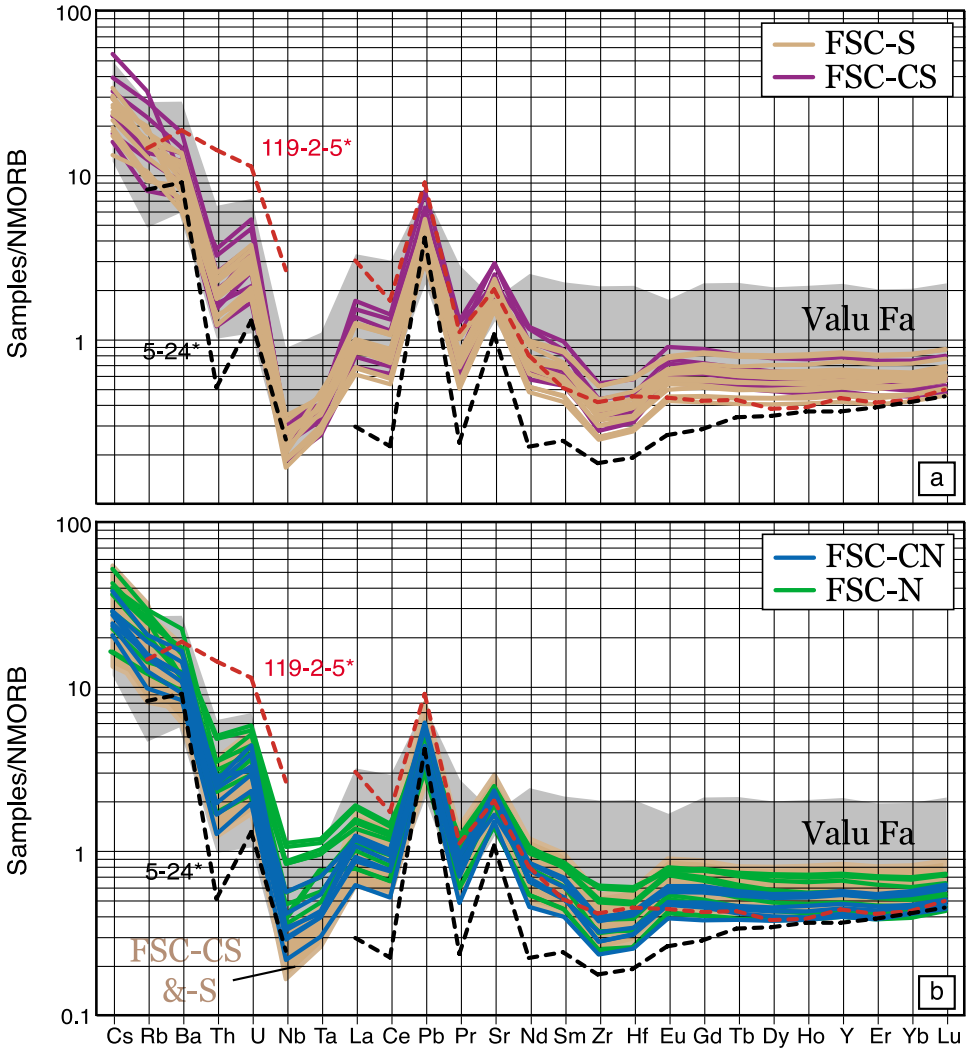

Figure 3. Trace element patterns normalized to N-MORB [*McDonough and Sun*, 1995]. The FSC-S and FSC-CS lavas show similar patterns, with highly incompatible element contents comparable to Valu Fa lavas and much lower heavy REE contents, reflecting a higher extent of melting. The FSC-CN and FSC-N lavas are distinguished by a progressive increase in Nb, Ta, La northward. The change is also associated with a steepening of the REE slope (e.g., higher La/Sm toward the north) requiring the presence of an enriched mantle (see text for details). 5–24* and 119-2-5* represent the depleted and intermediate boninitic end-members from *Falloon et al.* [2007], multiplied by 2 for the comparison and to compensate for the high MgO contents of these samples.

and from 38.200 to 38.520 for $^{208}Pb/^{204}Pb$. $^{87}Sr/^{86}Sr$ ratios vary from 0.703049 to 0.703713 and $^{143}Nd/^{144}Nd$ ratios from 0.512878 to 0.512998 (Figure 4). The isotope ratios generally correlate well with one another, and show some of the same features indicated by the trace element data. FSC-S and FSC-CS show a large range in isotope ratios, but the ratios do not vary systematically with distance from the strike of the arc. Moving northward, the FSC-CN and FSC-N have lower $^{143}Nd/^{144}Nd$, and FSC-N shows distinctly "enriched" values similar to some ocean island basalts in Sr, Nd and Pb and has little overlap with the more southerly segments. One sample (ND-63-01) from the FSC-CN displays the most extreme Pb isotopic composition associated with radiogenic $^{87}Sr/^{86}Sr$ and the lowest $^{143}Nd/^{144}Nd$ of the FSC-CN.

[27] The FSC isotope ratios differ greatly from those measured in the Eastern Lau Spreading Centers (Figure 4). The Pb and Sr isotope ratios overlap with the most radiogenic ELSC samples but also extend to significantly more radiogenic compositions. The

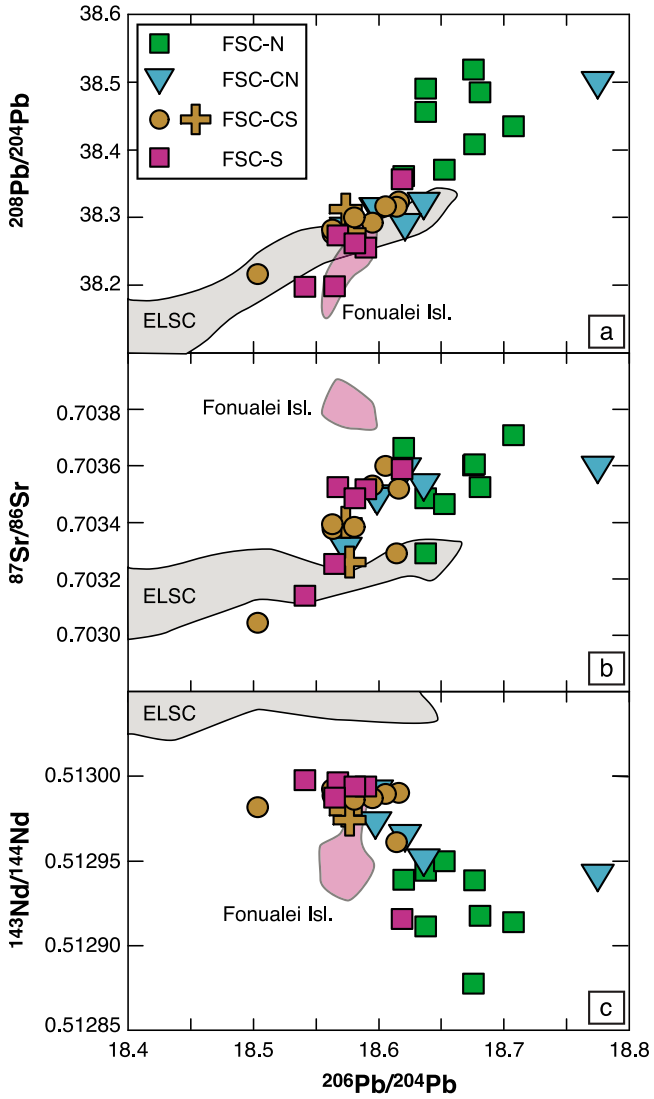

Figure 4. Isotope diagrams showing the range covered by the FSC samples and the relative position of the FSC groups. The fields for the ELSC [*Escrig et al.*, 2009] and Fonualei island [*Hergt and Woodhead*, 2007; *Pearce et al.*, 2007; *Escrig et al.*, 2009; *Turner et al.*, 2012] are also reported.

Nd isotope ratios have no overlap and are systematically lower [*Pearce et al.*, 1994; *Peate et al.*, 2001; *Pearce et al.*, 2007; *Escrig et al.*, 2009].

4.1. Removing the Effect of Low Pressure Crystallization

[28] In order to estimate the effects of melting and source variability on the major element contents, the data need first to be corrected for the effects of low-pressure fractionation. Previous works used constant slopes to correct the major element composition to 8 wt% MgO (or 6 wt%), often those from *Klein and Langmuir* [1987]. *Keller et al.* [2008] use the equations reported in *Taylor and Martinez* [2003] to correct their major element data for the FSC and MTJ.

[29] In our study, we use the equations reported by *Bézos et al.* [2009] that give the slopes for back-arc lavas to correct K_2O, Na_2O, TiO_2 and FeO back to 8 wt.% MgO. The slopes used for the corrections vary with the lavas' compositions, taking into account the effect of water in the melt. Water affects the relative appearance of minerals during magma differentiation by delaying the plagioclase relative to olivine and clinopyroxene, and changing the slope of the liquid lines of descent (LLD) [*Michael and Chase*, 1987; *Sinton and Fryer*, 1987; *Danyushevsky*, 2001; *Asimow and Langmuir*, 2003].

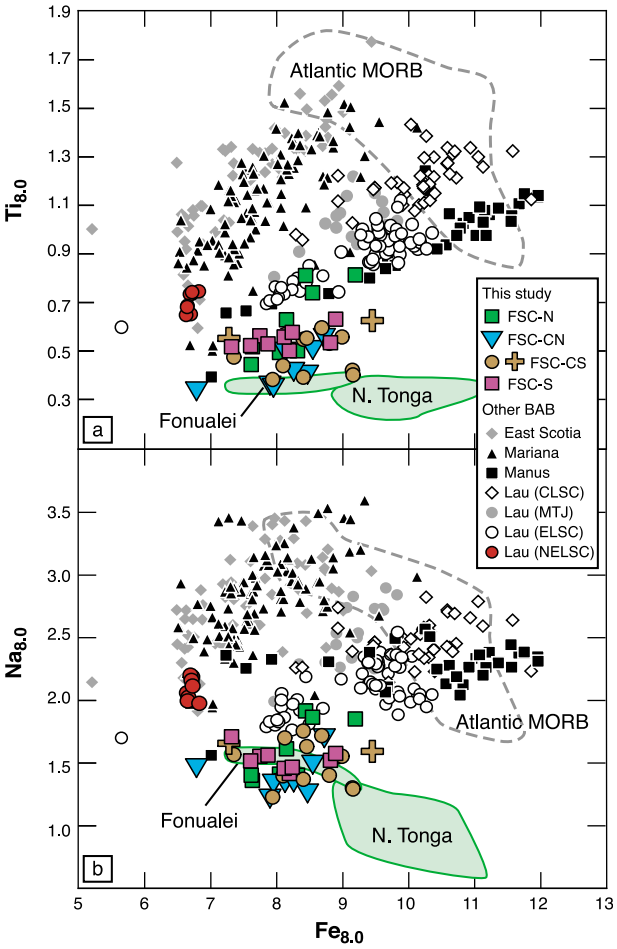

Figure 5. $Na_{8.0}$ and $Ti_{8.0}$ versus $Fe_{8.0}$ diagrams, modified from *Langmuir et al.* [2006]. We report the corrected data for the FSC, for the NELSC [*Falloon et al.*, 2007] and for the nearby Tonga islands [*Turner et al.*, 1997; *Ewart et al.*, 1998; *Hergt and Woodhead*, 2007; *Pearce et al.*, 2007; *Regelous et al.*, 2008]. Our new data set is characterized by the extremely low $Ti_{8.0}$ and $Na_{8.0}$ values, as well as low $Fe_{8.0}$. Low $Ti_{8.0}$ and $Na_{8.0}$ are interpreted to reflect high extent of melting, which is consistent with the low HREE contents (see Figure 3).

[30] Determining when plagioclase and clinopyroxene appear is another critical feature for making an accurate correction. Based on the location of kinks in the MgO versus Al_2O_3 and versus CaO diagrams, and on petrological observations, we can estimate when plagioclase and clinopyroxene start to crystallize for each group (FSC-S: 7.15% for plag and >7.5% for cpx ; FSC-CS: 7.0% for plag and 7% for cpx; FSC-CN: 6.5% for plag and 6.9% for cpx; FSC-N: 6.65% for plag and 7.25% for cpx; MTJ: >8.3 for plag and >8.3 for cpx). For the elements we want to correct (not CaO), the presence of cpx has little effect on the LLD slopes so we chose to correct the data back to MgO_{plag} and then add olivine back to 8% MgO. Looking at the glass chips, we can assess the presence of the minerals and validate when the plagioclase comes in. Except for a couple of samples, there is a very good consistency within each group. The most differentiated samples contain plagioclase while the less differentiated samples do not. Our correction method produces slightly higher $Fe_{8.0}$, $Ti_{8.0}$ and $Na_{8.0}$ values relative to the corrected data from *Keller et al.* [2008] as they did not use variable and lower MgO contents for the plagioclase appearance.

[31] A similar method is applied to the Fonualei, Tafahi and Niuatoputapu island lavas. Determining when plagioclase starts crystallizing is harder for the Tonga arc lavas due to the absence of a continuous range of MgO values. By combining data for lavas from the three islands, we can estimate that plagioclase comes in at MgO ~ 4.5%, and correct the lavas with MgO > 2%. For Fonualei, only a few samples are not dacite and the MgO is comprised between 2.4 and 3.1%. Despite the large correction applied and the uncertainties on the slopes and when plagioclase comes in, the $Ti_{8.0}$ and $Na_{8.0}$ values calculated are higher for Fonualei lavas than the N. Tonga island values, consistent with the lava compositions (Figure 2). Boninitic samples from the literature with high MgO content are not corrected as they reflect olivine phenocryst accumulation that may not be at equilibrium with the lavas [*Falloon et al.*, 2007].

[32] The major element data corrected back to 8% MgO are reported in Figure 5 together with the corrected data from the other Lau Spreading Centers [*Langmuir et al.*, 2006; *Falloon et al.*, 2007; *Bézos et al.*, 2009] and from Mariana, Manus and East Scotia back-arc basins [*Langmuir et al.*, 2006]. The FSC groups contain the lowest $Ti_{8.0}$ and $Na_{8.0}$ measured in back-arc lavas ($Ti_{8.0}$ ~ 0.35% and $Na_{8.0}$ ~ 1.23%) and plot significantly below the trend defined by the Lau-ELSC and Manus trend, offset toward the fields of Fonualei, Tafahi and Niuatoputapu Islands (Figure 5). Only a few samples from the FSC-N overlap with the Lau-ELSC trend.

[33] Samples from the Northeast Lau Spreading Center [*Falloon et al.*, 2007] have higher $Ti_{8.0}$ and $Na_{8.0}$ and plot at the hydrous extremity of the Mariana or East Scotia trends suggesting either lower mantle temperature and/or a more enriched source.

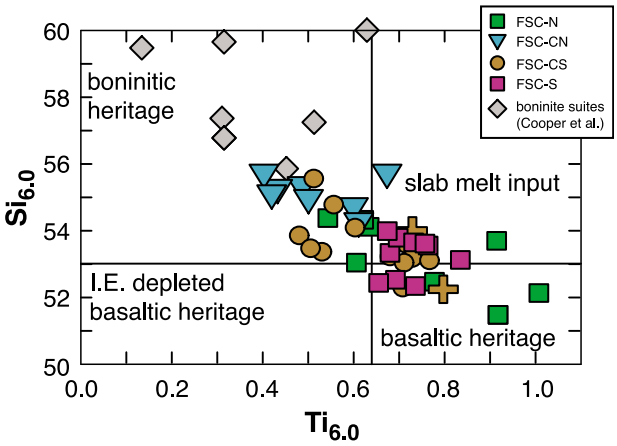

Figure 6. $Si_{6.0}$ versus $Ti_{6.0}$ diagram, modified from *Cooper et al.* [2010]. The corrected data reveal that the FSC-CN and part of the FSC-CS and FSC-N samples have a boninitic signature as defined by *Cooper et al.* [2010]. The other samples extend along the same trend toward the basaltic heritage domain. Note that this figure is way to compare our samples (MgO values between 6 and 8%) with boninites found in the NE corner of the Lau Basin which differ greatly in major element composition due mostly to olivine accumulation [*Danyushevsky et al.*, 1995; *Falloon et al.*, 2007, 2008].

4.2. Characterization of a Boninitic Signature

[34] Apart from their MgO contents, the FSC glasses have boninitic characteristics such as low TiO_2 (<0.5%) and high SiO_2 (>53%) as defined by *Crawford et al.* [1989]. In order to directly compare our glass analyses with the whole rock characteristics that define boninites, we have corrected the SiO_2 and TiO_2 contents to 6% MgO and plotted them in a simplified version of the figure that *Cooper et al.* [2010] propose as an indicator of a boninitic signature (Figure 6). Notably, FSC-CN plots almost entirely within in the boninitic heritage field, FSC-CS straddles the basaltic and boninitic heritage fields, and FSC-S plots entirely in the basaltic heritage field, although it is closest to the arc. The two highest MgO samples show no evidence for plagioclase or clinopyroxene crystallization (Figure 2) and have high CaO/Al_2O_3 values ~0.725 and 0.777 typical of high Ca boninites observed in the N. Tonga [*Falloon and Crawford*, 1991; *Danyushevsky et al.*, 1995] and further south [*Cooper et al.*, 2010].

4.3. Hydrous End-Member

[35] The degassing of H_2O that affected our samples does not allow a direct comparison of the corrected water and major element data in order to characterize a hydrous end-members as done by *Langmuir et al.* [2006] and *Bézos et al.* [2009]. It can however be inferred by combining trace element data (Figure 7) and corrected major element data. The tight correlation defined by the FSC in the $Ti_{8.0}$-$Na_{8.0}$-Ce/Pb plots (Figure 7), similar to the one defined by the ELSC1 [*Bézos et al.*, 2009], requires the involvement of an arc-like end-member with low Ce/Pb, $Ti_{8.0}$ and $Na_{8.0}$ and an end-member with

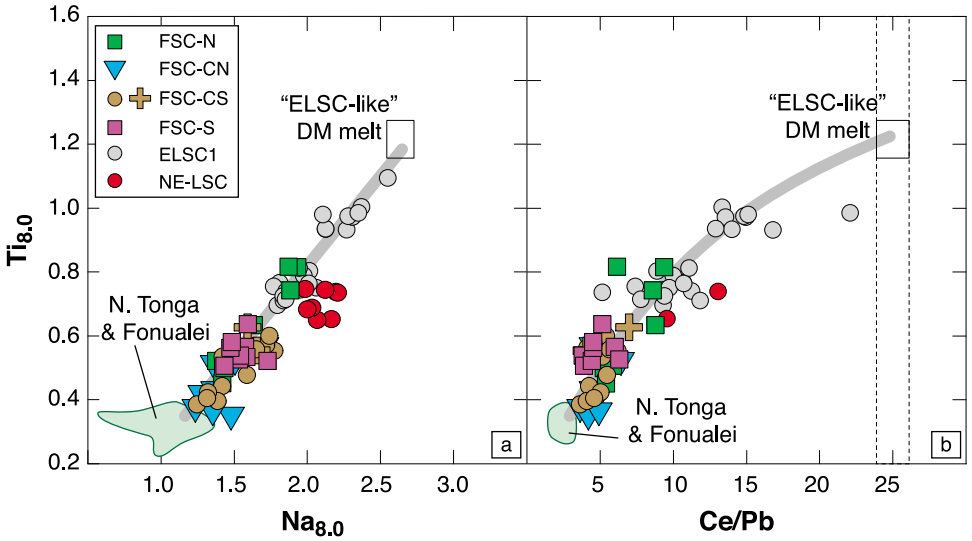

Figure 7. $Ti_{8.0}$ versus $Na_{8.0}$ and Ce/Pb diagrams. The trend defined by the FSC lavas extends the trend defined by the ELSC1 segment [*Bézos et al.*, 2009], from a ELSC-like DM end-member toward the Tonga island field. To first order, low Ce/Pb can be used as a proxy for the amount of subduction input and suggests that the high extent of melting (low $Ti_{8.0}$ and $Na_{8.0}$) is related to the amount of water/subduction input to the mantle wedge.

higher Ce/Pb, $Ti_{8.0}$ and $Na_{8.0}$, possibly MORB-like with a canonical Ce/Pb value of 25 [*Hofmann et al.*, 1986] and high $Ti_{8.0}$ (~1.2) and $Na_{8.0}$ (~2.6). Previous studies [*Langmuir et al.*, 2006; *Bézos et al.*, 2009] have attributed the low $Ti_{8.0}$-$Na_{8.0}$-Ce/Pb compositions of Lau back-arc lavas to hydrous melts associated with the release of fluid-rich components from the slab. This is consistent with the Ce/Pb variation, which can be used as a proxy for the fluid addition to the mantle wedge.

4.4. Along-Axis Variation and Comparison With the Arc Lavas

[36] Characterizing spatial geochemical changes along the FSC is critical for understanding the nature of the processes responsible for the lavas variability. Within the FSC itself, there is substantial major and trace element variability that changes systematically but not simply from south to north (Figure 8). In Figure 8, for $Ti_{8.0}$, and ratios sensitive to the addition of a subduction component (fluid or melt), we define a "baseline" going through the samples least affected by the subduction input within a given latitude span (±0.15°). This baseline provides a reference for a regional gradient from which local variations can be distinguished. The local variation likely reflects localized contributions of the subduction input to the melting regime beneath the spreading center [*Escrig et al.*, 2009]. The projected locations of the arc volcanoes on the spreading center are also reported in order to check any correlation between the locations of the arc volcanoes and where the strongest contribution of the subduction input is seen along the spreading center. The volcanoes' locations have been projected using the azimuth given by *Zellmer and Taylor* [2001] for the plate motion (109°), which gives a projection perpendicular to the arc front.

[37] $Ti_{8.0}$ shows little variation in the FSC-S, decreases northward along the FSC-CS to reach a minimum between the FSC-CS and -CN, and increases to reach a maximum in the FSC-N area. Trace element ratios sensitive to a fluid-rich subduction component show a similar variation north of 17.5°S, with increasing Ba/Nb, and decreasing Ce/Pb with decreasing $Ti_{8.0}$ (Figure 8). Overall, the three most southerly segments display relatively similar enrichment in fluid-mobile elements despite the variation in distance from the arc volcanic front. The FSC-S only shows an enrichment stronger than the FSC-CS and -CN at its southern end (south of 17.5°S), near Fonualei island (Figure 8). Trace element ratios sensitive to a sediment-melt contribution (e.g., Th/Nb) decrease northward. Th/Nb show offsets from the baseline, toward higher values, slightly less pronounced than the ones defined by the ratios sensitive to fluid-mobile addition (Figure 8). These offsets from the baseline observed using ratios sensitive to fluid-addition and to a lesser extent, ratios sensitive to a sediment melt addition, represent localized increases in subduction input characterized by high Ba/Nb and Th/Nb, and low Ce/Pb, and support that the subduction component is mostly fluid-dominated with a small sedimentary contribution responsible for the high Th/Nb.

[38] The comparison with the Tonga arc lavas shows that the trace element ratios tracking the enrichment in fluid-mobile elements of the FSC lavas (Ce/Pb and Ba/Nb) reflect a decrease of the subduction input with the increasing distance from the arc front (lower Ba/Nb and higher Ce/Pb in the back-arc lavas). This result is similar to what has been observed in the ELSC [*Escrig et al.*, 2009].

[39] Trace element ratios such as Nb/Zr and La/Sm show evidence for another kind of trace element enrichment, including incompatible HFSE elements that should be little influenced by a fluid-dominated subduction component. Using the same approach as described above, we define a baseline using the samples with the lowest Nb/Zr within a given latitude interval. For Nb/Zr there is a clear change in baseline, with the ratio near 0.02 south of 17°S, and increasing progressively to >0.04 in the north. Individual Nb/Zr ratios do not appear to deviate much from the baseline, indicating as expected that this ratio is not significantly influenced by the subduction components that are clearly identified in ratios such as Ba/Nb and Ce/Pb. (Figure 8). This is also evident from the fact that the variation in Nb/Zr correlates negatively with Th/Nb, La/Nb and Ba/Nb, and does not correlate with Ce/Pb (Figure S3). Significantly, the latitudinal compositional change in Nb/Zr is similar in both the back-arc and arc lavas, suggesting that the mantle wedge composition is changing northward with no relationship with the distance from the arc or the depth of the slab.

[40] The $^{206}Pb/^{204}Pb$, and $^{143}Nd/^{144}Nd$ overall latitudinal variations are quite similar to the Nb/Zr variation (Figure 8). $^{143}Nd/^{144}Nd$ shows no variation within the FSC-S and FSC-CS, except for the northernmost sample of the FSC-S which also has a particularly high Th/Nb, strongly contrasting with the other samples (Figure 8). $^{143}Nd/^{144}Nd$ then decreases regularly toward the north. A similar decrease is seen in the arc lavas. $^{206}Pb/^{204}Pb$ displays a similar overall variation, reaching maximum values

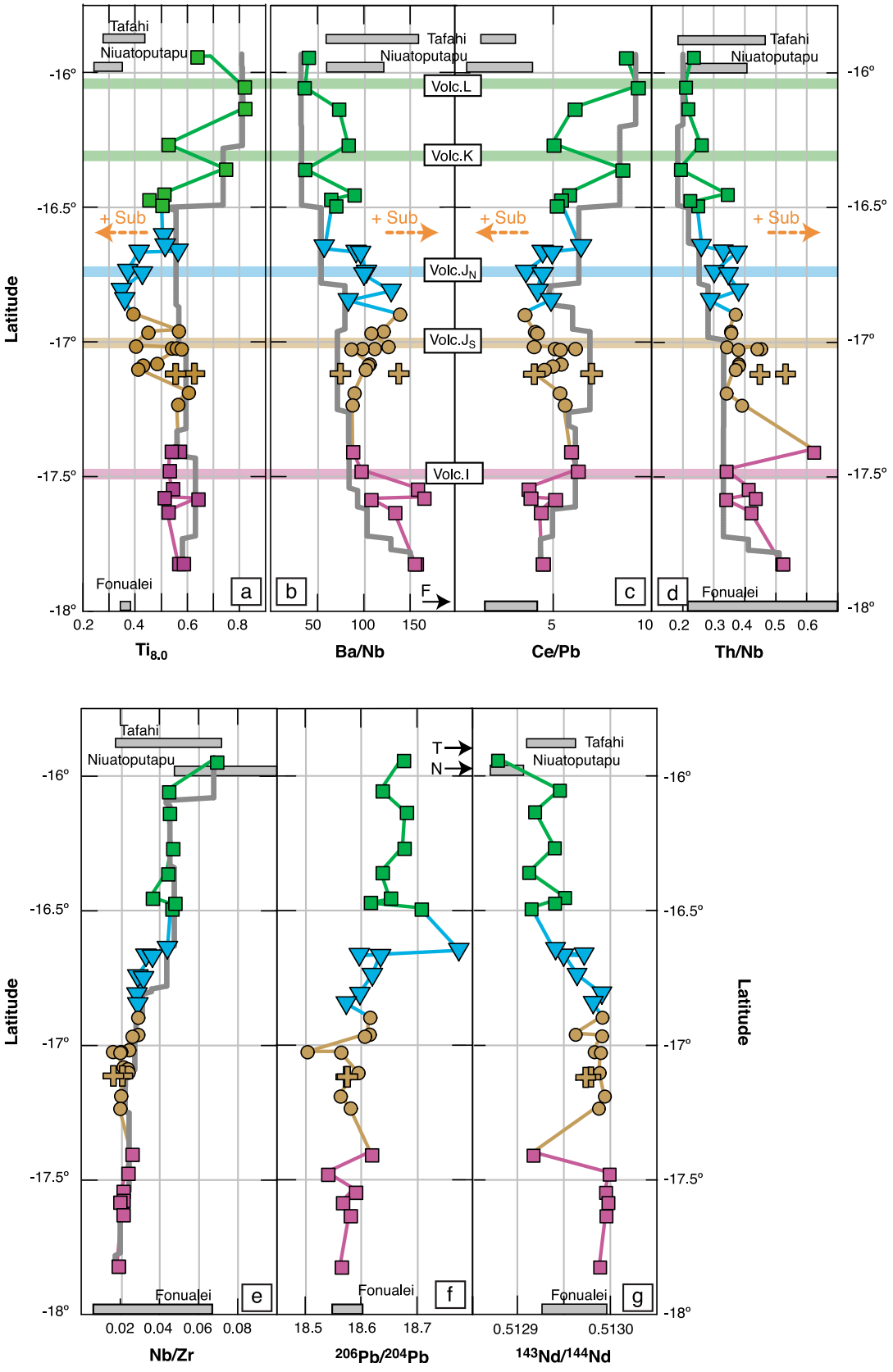
Tafahi
Niuatoputapu
Fonualei
Volc.L
Volc.K
Volc.J_N
Volc.J_S
Volc.I
+ Sub
F
T
N
a
b
c
d
e
f
g
-16°
-16.5°
-17°
-17.5°
-18°
Latitude
Ti8.0
Ba/Nb
Ce/Pb
Th/Nb
Nb/Zr
206Pb/204Pb
143Nd/144Nd

Figure 8

in the FCS-N, requiring that the source of the high Nb/Zr has radiogenic $^{206}Pb/^{204}Pb$.

[41] The Sr isotopes appear to be influenced by both this background enrichment and subduction processes. The $^{87}Sr/^{86}Sr$ latitudinal variation (not shown) shows a slight increase toward the north, which would be akin to the change observed for Nd and Pb isotopes. The significant range of variation within a group compared to the overall range makes it difficult to distinguish, but peaks of radiogenic $^{87}Sr/^{86}Sr$ can be found at the same latitude as the peaks defined by the trace element ratios sensitive to an enrichment in fluid mobile elements.

[42] The projected locations of the arc volcanoes on the spreading center show that, for the FSC-CS and -CN, there is a good correspondence between projected locations and peaks in subduction input identified using Ba/Nb and Ce/Pb and to some extent Th/Nb (Figure 8). Further north, in the FSC-N, the projected location of volcano K also corresponds to a peak characterized by low $Ti_{8.0}$, Ce/Pb and high Ba/Nb and Th/Nb. In the south, closer to the arc (FSC-S), the projected location of volcano I is slightly offset to the north (~10 km) of the peaks in Ba/Nb and Ce/Pb. There is a large bathymetric anomaly at the projected location (Figure 1), however.

[43] The data indicate therefore that two principal factors contribute to the latitudinal variations- a change in the composition of the background mantle as indicated by Nb/Zr and the isotope data, and the subduction influence that changes progressively northward but is also punctuated by peaks corresponding to projected position of volcanoes of the Tonga volcanic front.

5. Discussion

[44] The combination of the major element, trace element and isotope data allow us to develop a petrogenetic model for the complex signatures observed in the FSC lavas. It is also instructive to compare the Fonualei Spreading Center with the Eastern Lau Spreading Center located further south, and with the boninitic samples found in the NE Lau Basin [*Danyushevsky et al.*, 1995; *Falloon et al.*, 2007, 2008].

5.1. Origin of the Enriched Mantle Component

[45] The trace element and isotopic data discussed above demonstrate two sources of enrichment: an OIB-like component and a fluid-rich component similar to the one added to the Tonga arc source (see section 5.2). The first process is characterized by an enrichment in all incompatible elements (not just the mobile elements) and can be separately tracked using ratios that are less influenced by a fluid-rich subduction component (e.g., Nb/Zr and La/Sm). We address first the question of the origin of this regional enrichment gradient.

5.1.1. An Enrichment Decoupled From Recent Subduction Input

[46] As discussed in the previous section, the compositional change tracked by Nb/Zr and La/Sm does not correlate with the fluid-rich subduction component (e.g., Ce/Pb). In order to more fully characterize this enrichment, we can use $Nb_{8.0}$ and $Zr_{8.0}$ values, which are primarily sensitive to the enrichment of the mantle source and the degree of melting. The Nb/Zr ratio reflects the source as long as the extent of melting is greater than ~10%. For constant Nb/Zr, Nb and Zr vary with extent of melting. In the northern Lau Basin, the back-arc and arc lavas show a similar increase in Nb/Zr with latitude. For example, the FSC-N has comparable Nb/Zr to the N. Tonga islands.

[47] Since there is no variation in the Nb/Zr ratio across arc, and no correlation of Nb/Zr with chemical indices of subduction, it is evident that the *source* variations are not related to current subduction. The subduction influence is apparent, however, in the element concentrations. Along the

Figure 8. Latitudinal variation of key geochemical proxies tracking the amount of subduction input and the presence of an enriched mantle. Thick gray lines represent baselines defined by the on-axis samples. The colored horizontal lines represent the projection of the location of the arc volcanoes on the spreading center (perpendicular to the arc front). Significant offsets from the baseline reflect local increases in the amount of subduction component added to the back arc mantle source. Note that the offsets in $Ti_{8.0}$, Ba/Nb and Ce/Pb either correspond to (or are very close to) the projected locations of the arc volcanic edifices. Close to the arc front, the back-arc lavas have compositions that are geochemically quite similar to the Tonga arc lavas (e.g., Ce/Pb and $^{206}Pb/^{204}Pb$), while further away the back arc lavas show less enrichment in mobile elements. Nb/Zr variation is tracking the presence of an enriched mantle source. It increases progressively toward the north, and an increase is also seen in the Tonga arc lavas requiring that the change in Nb/Zr is affecting the entire mantle wedge and unrelated to a subduction related process. A similar result is shown by the $^{143}Nd/^{144}Nd$ ratio that decreases northward in both the arc and back-arc lavas.

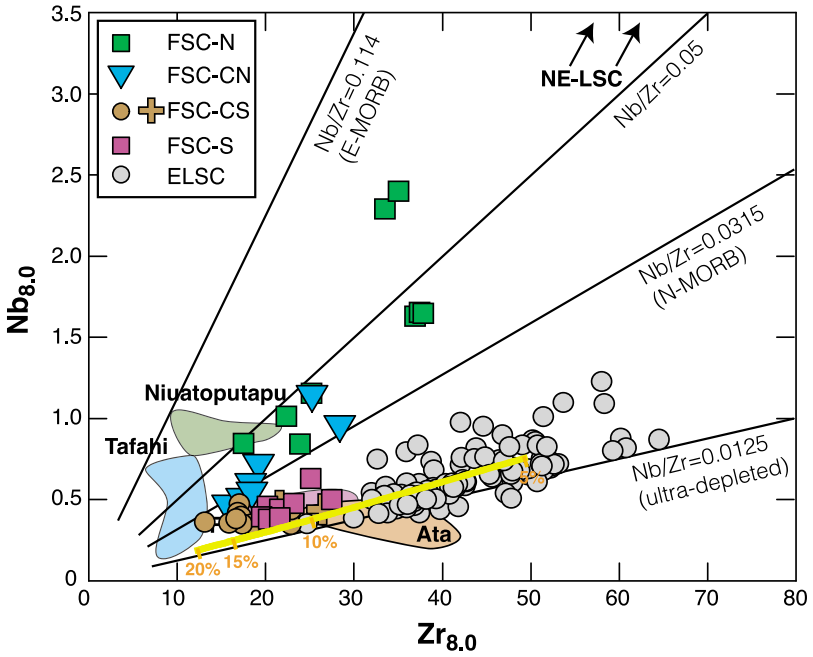

Figure 9. $Nb_{8.0}$ versus $Zr_{8.0}$ diagram. The change in $Nb_{8.0}$ and $Zr_{8.0}$ reflects the enrichment of the mantle source and to some extent the degree of melting. The effect of melting is represented by the yellow curve (F ranging from 5% to 20%, using the depleted source), which shows that the difference between the FSC groups is mostly due to source variation. The Nb/Zr ratio can be used as a proxy for the enrichment of the mantle source, unaffected by the subduction input. It shows that the FSC mantle source is more enriched toward the north. The source of the N. Tonga islands (Tafahi and Niuatoputapu) is also more enriched than the mantle source beneath Fonualei or Ata islands. The FSC source is also more enriched than the ELSC mantle source. At a given Nb/Zr value, low $Nb_{8.0}$ and $Zr_{8.0}$ reflect higher extent of melting. Arc lavas are produced by higher extents of melting than the back-arc lavas.

entire length of the subduction zone, the arc lavas have lower $Nb_{8.0}$ and $Zr_{8.0}$, than the adjoining back-arc (Figure 9). This is consistent with higher extent of melting for the arc than the back-arc, owing to their higher water contents. Therefore the subduction influence increases extent of melting, and acts upon a pre-existing source gradient.

[48] The question remains, however, whether some past subduction influence could have caused this regional enrichment, or whether it reflects the presence of an enriched mantle flowing southward, possibly related to a mantle plume (e.g., Samoa as proposed by *Falloon et al.* [1992]; *Danyushevsky et al.* [1995]; *Turner and Hawkesworth* [1998]; *Falloon et al.* [2007]; *Falloon et al.* [2008]; *Regelous et al.* [2008]; *Lupton et al.* [2009]; and *Tian et al.* [2011]). Possible subduction-related candidates for the origin of the high-Nb component are the subducted Louisville Seamounts chain and the associated volcaniclastic sediments. Both have high Nb contents and have been proposed to significantly contribute to the trace element budget of the N. Tonga arc lavas [*Regelous et al.*, 1997; *Turner et al.*, 1997; *Regelous et al.*, 2010].

[49] In order for these sediments or seamounts to contribute enough Nb, the contribution would have to come in the form of a sediment melt, bulk sediment or partial melt of the slab, since Nb is not fluid mobile. But in that case a problem arises with Ce/Pb, since the volcaniclastic sediments, and almost certainly the Louisville seamounts, have high Ce/Pb relative to the subduction related lavas. Also, because this subduction zone has the highest convergence rate in the world, the slab has the coolest temperatures globally, and would be least susceptible to slab melting.

[50] Isotope data provide additional constraints. Due to the difference in mobility between Sr and Nd, $^{143}Nd/^{144}Nd$ is almost insensitive to fluid addition relative to $^{87}Sr/^{86}Sr$. A significant $^{87}Sr/^{86}Sr$ variation with no $^{143}Nd/^{144}Nd$ variation is indicative of fluid addition. Alternatively, a combined variation in both isotope ratios reflects either solid-solid mixing (e.g., enriched mantle mixing with a depleted mantle) or the addition of a melt to the mantle source (e.g., sediment melt). The variation in the mantle wedge would plot at the lowest $^{87}Sr/^{86}Sr$ for given $^{143}Nd/^{144}Nd$.

[51] Figures 11 and 12 illustrate these principles. An appropriate baseline (shown as an orange line) for the wedge can be constructed by mixing of depleted mantle with an enriched mantle end-member similar to sample 119-2-5 from *Falloon et al.* [2007], recovered in the northern part of the Lau Basin (see further discussion of 119-2-5 in subsequent sections). The FSC mantle wedge would be intermediate between these two end-members. Deviation from this mixing line would then reflect the contribution of the fluid-dominated subduction input. FSC-S and -CS display almost no $^{143}Nd/^{144}Nd$ variation despite a large range in $^{87}Sr/^{86}Sr$ consistent with a hydrous melt end-member with a composition similar to the Fonualei island lavas (Figure 11). The contribution of the enriched mantle in the FSC-CN and -N is characterized by lower $^{143}Nd/^{144}Nd$ and higher $^{87}Sr/^{86}Sr$ along the mixing baseline. Indeed, the three FSC-N samples plotting near the proposed wedge mixing curve have the lowest Ba/Nb and highest Ce/Pb values. The other four FSC-N samplesoffset toward high $^{87}Sr/^{86}Sr$ at a given $^{143}Nd/^{144}Nd$, and Tonga island fields, create the spikes in subduction input in the latitudinal plots. A similar line of reasoning can be carried out in the other isotope spaces (Figure 12).

[52] Note also that the N. Tonga lavas for which Louisville Seamounts or volcaniclastic sediment contribution have been proposed [*Regelous et al.*, 1997; *Turner et al.*, 1997; *Regelous et al.*, 2010] have characteristics that would be consistent with a fluid from these sources, not a melt. That fluid might then account for the high Pb isotopes at the same time as low Ce/Pb and high Ba/Th. That contribution would not be the cause of the high Nb, however.

[53] An alternative mixing end-member might be a combination of bulk pelagic sediment with a volcaniclastic component to get an appropriate trace element and isotopic composition. Polluting the mantle wedge with such a component would require some special pleading, however: 1- the enrichment agent derived from the subducted slab would have to be different from the slab contribution currently expressed in the N. Tonga lavas and derived from the same subducted materials; 2- it would need to be regularly more pronounced in the FSC lavas located further away from the arc and further north; and 3- it would have to have happened prior to the addition of the fluid-dominated subduction input and after the beginning of the Lau basin opening.

[54] Therefore we consider it unlikely that the source of the Nb enrichment northward reflects a subduction influence. The low Ce/Pb and high Ba/Th would require a fluid from the sediment. But the fluid would not carry Nb to account for the Nb enrichment. On the other hand, bulk mixing of the sediment or a sediment melt might carry sufficient Nb, but then would not account for the fluid signature. It is more likely that the origin of the enrichment in Nb toward the north is an enriched mantle flowing southward, possibly affected by a subduction flavor in its history (to account for the low Ce/Pb), and that the change in Nb/Zr reflects a progressive change in the background mantle composition.

5.1.2. Origin of the Enriched Mantle

[55] Previous studies of the lavas erupting in the Northern Lau Basin have also identified mantle wedge enrichment, which has been ascribed to diverse processes [*Regelous et al.*, 1997; *Turner et al.*, 1997; *Turner and Hawkesworth*, 1997; *Wendt et al.*, 1997; *Ewart et al.*, 1998]. Most recently, *Falloon et al.* [2007] identified multiple enriched mantle components in the N. Tonga lavas, the back-arc lavas and the boninites. *Falloon et al.* [2007] proposed a complicated quantitative model involving multiple components, but limited to the Sr, Nd and one Pb isotope ratio (thus not using the strong constraints brought by the linearity of mixing in Pb-Pb isotope diagrams). They proposed three end-members: depleted, intermediate and enriched in trace element compositions.

[56] In the case of the *Falloon et al.* [2007] samples, these end-members are associated with boninites. It is important to separate the trace element and isotopic characteristics of the source, however, from the particular major element characteristics that define boninites. We address further below the melting conditions that are necessary for boninite genesis. At this point we consider only the trace element and isotopic characteristics of the *Falloon et al.* [2007] end-members.

[57] *Falloon et al.* [2007] attributed the origin of the *enriched* component to a melt derived from a combination of mantle components (HIMU, EMI and EMII). They also proposed another plume-related component for their *depleted* end-member, a refractory OIB mantle source that melts when fluxed by a fluid-rich subduction component. The *intermediate* end-member, represented by sample 119-2-5, they ascribed to a mixture between a refractory OIB source and an enriched melt derived

from a mixture of OIB components. Sample 119-2-5 is characterized by high La/Sm (close to 6), low Ba/Nb, Ce/Pb and Ba/Th relative to the FSC and N. Tonga lavas. The slight enrichment in fluid mobile elements suggests that the enriched melt responsible for the OIB-like enrichment may also carry a small enrichment in mobile elements.

[58] For the Fonualei Spreading Center, the incompatible trace element and isotope ratios require the involvement of only a single enriched mantle component, and an appropriate isotopic composition is the *intermediate* end-member (sample 119-2-5). As illustrated in Figures 10–12, the geochemical variations of the FSC samples can be accounted for by creation of diverse mantle wedge compositions generated by mixing sample 119-2-5 with depleted source, then modified by a subduction component represented by the arc fields. The FSC samples that plot on the trend between the depleted source and sample 119-2-5 are those with the lowest enrichment in fluid-mobile elements. This is consistent with creation of a mantle wedge gradient prior to the addition of the subduction input.

[59] Since the chemical characteristics of sample 119-2-5 seem to play an important role in this region, the origin of these chemical characteristics needs to be considered. Starting from Falloon's interpretation, we propose that the enriched mantle component is created by an OIB-like refractory mantle source (e.g., depleted in major elements), possibly related to the Samoan plume, that has been re-enriched by a metasomatitic agent that includes both a low-F melt and fluid signatures. Indeed, in many diagrams (Figures 10–12), 119-2-5 is located between the Samoan island field (e.g., Upolu post erosional) and the N. Tonga islands. A low-F melt derived from a Samoan component and a subduction-related fluid similar to the one contributing to the N. Tonga lavas could explain the trace element and isotopic signature of the enriched mantle component.

[60] In summary, we propose that the enriched mantle source is a previously depleted refractory mantle that has been re-enriched in trace elements by a low-F melt derived from a Samoan component, which then crossed the trench-transform boundary flowing southward. To account for its slightly low Ce/Pb ratio, it must also have received a slight subduction component. The mixture of the depleted mantle wedge with this metasomatized enriched mantle makes a complex background component that provides the material that has been recently influenced by current subduction to create the strong arc-signature and spatially organized arc-like enrichments. With a complex history involving OIB and multiple arc components, this region is exceptionally complex on a global basis.

5.2. Characterization of the Recent Subduction Input and Comparison With the Tonga Arc Volcanoes

[61] The data from this region support a spatial correspondence between the subduction input reflected in the back-arc lavas and the location of the arc volcanoes, as was also evident along the ELSC [*Escrig et al.*, 2009]. The FSC-S, FSC-CS and most of the FSC-CN either overlap with (or define a trend pointing toward) the field of Fonualei island, (Figures 10–12), which can be thus used as a proxy for the subduction-related end-member. To the north, the FSC-N defines a distinct trend in Figures 10–12 toward a subduction-related end-member (see Table S2) that is intermediate between Fonualei and the northern island Tafahi (Figure 1). One notable sample, ND-63-01 from the FSC-CN, is shifted more than any other FSC lava toward the northern islands.

[62] In the south where there is available data on the arc composition, there is a clear geochemical relationship between the subduction input added to the arc and the corresponding back-arc magma sources. Geochemical data for the submarine volcanoes in the north sampled during the R/V Southern Surveyor cruise SS11/04 will ultimately reveal if the composition of the subduction input is changing similarly along the arc front and the spreading center.

[63] The local increases ('peaks') in trace element ratios that are sensitive to the addition of a fluid-rich subduction input (Figure 8) correspond relatively well spatially to the projected location of the arc volcanoes on the spreading center. In detail, the correspondence is not perfect. Close to the arc front, within the FSC-S, the projected location of the volcano "I" is a few kilometers north of the apparent peak in subduction component (Figure 8). The offset is however not very significant and additional samples could help to better define the location of the peak. Further north, the increases in subduction input within the FSC-CS and -CN do correspond to the projected locations of volcano "J" (south and north). The projected location of volcano "K" is also near a peak of subduction input within the FSC-N (Figure 8).

[64] Several mechanisms could explain the spatial and geochemical coupling between the arc and

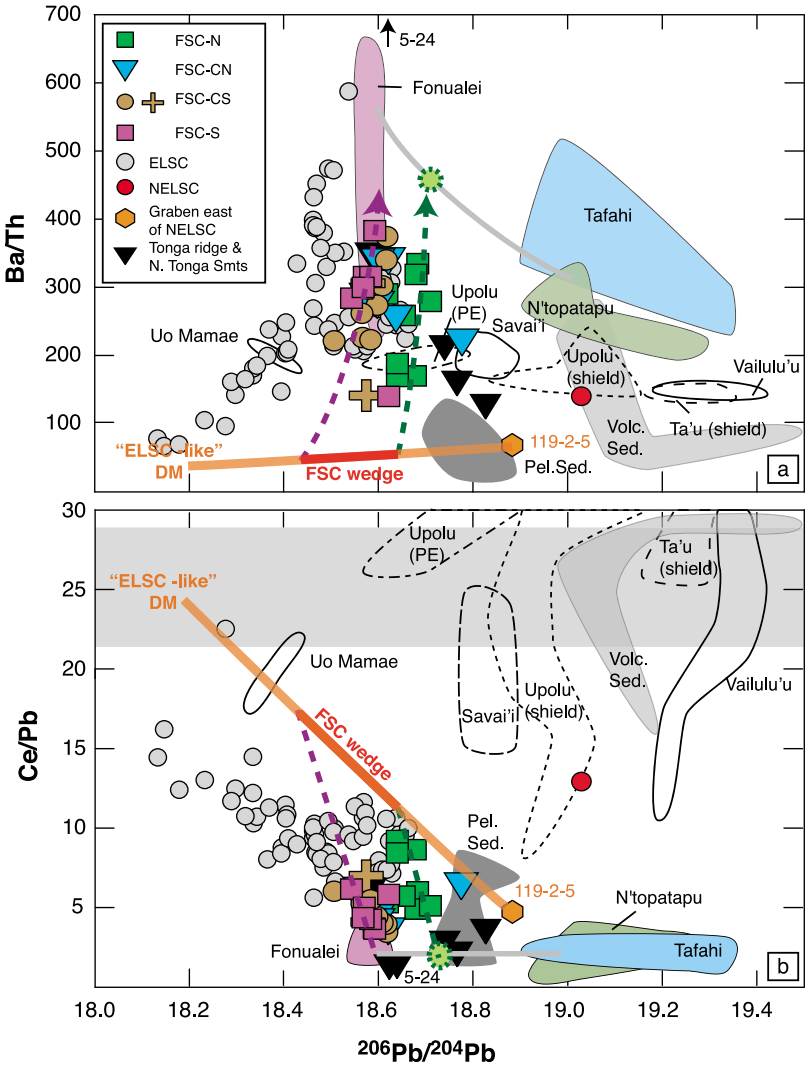

Figure 10. Ce/Pb-Ba/Th versus $^{206}Pb/^{204}Pb$ diagrams. The FSC data appear together with the NELSC [*Falloon et al.*, 2007], the ELSC [*Escrig et al.*, 2009], Tonga arc lavas [*Jenner et al.*, 1987; *Turner et al.*, 1997; *Ewart et al.*, 1998; *Hergt and Woodhead*, 2007; *Pearce et al.*, 2007; *Escrig et al.*, 2009], submarine samples from the Tonga ridge and N. Tonga seamounts [*Falloon et al.*, 2007], pelagic and volcaniclastic (associated with the Louisville Seamount Chain) sediments [*Turner et al.*, 1997] and Samoan island lavas [*Palacz and Saunders*, 1986; *Wright and White*, 1987; *Farley et al.*, 1992; *Workman et al.*, 2004; *Jackson et al.*, 2007, 2010]. The orange line shows mixing between depleted mantle and an enriched mantle end-member (119-2-5) characteristic of this region. FSC ridge segments plot on quasi-linear trends. One end shows a progressive enrichment toward the north in the mantle wedge, reflected by the change in intersection of the depleted mantle/enriched mantle mixing line. The other shows a change in subduction input that follows the corresponding variation in the Tonga arc. The FSC-S, FSC-CS and to some extent the FSC-CN define trends toward the Fonualei island field, while the FSC-N defines a trend toward an end-member (green filled dashed circle) intermediate between Fonualei and Tafahi.

back-arc. Close to the arc front, the subduction component in the back arc might have a common origin and pathway as in the arc volcanoes. This hypothesis is supported by the fact that the back-arc is currently capturing the subduction input [*Keller et al.*, 2008] and by the similarity between Fonualei island lavas and the nearby FSC samples. But it is hard for this mechanism to account for the similarity in back arc volcanoes that are far from the arc front because this would seem to require distant lateral migration of fluids in the mantle wedge.

[65] An alternative hypothesis that can also explain the spatial correspondence is that the subduction components are focused into the mantle wedge owing to 3-D effects on mantle flow. One of the long-standing observations of arc volcanism is the

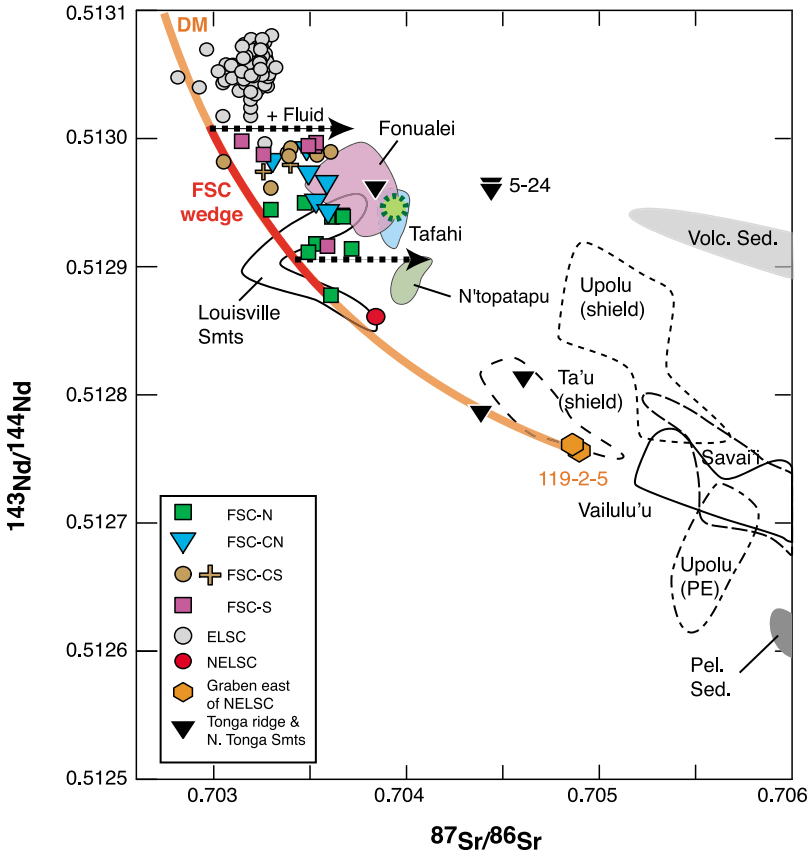

Figure 11. $^{87}Sr/^{86}Sr$ versus $^{143}Nd/^{144}Nd$ diagram illustrating the effect on the isotopic composition of the enriched mantle and the addition of a subduction component. The southernmost FSC groups (FSC-S and -CS) display almost no variation in $^{143}Nd/^{144}Nd$ despite significant variation in $^{87}Sr/^{86}Sr$. This reflects mostly the addition of a subduction component dominated by fluid (and thus containing negligible Nd). The increase in $^{87}Sr/^{86}Sr$ associated with a decrease in $^{143}Nd/^{144}Nd$ reflects an increasing proportion of enriched mantle. The latter cannot be related to either a sedimentary contribution (pelagic or volcaniclastic [*Turner et al.*, 1997; *Ewart et al.*, 1998]) or the Louisville Seamount Chain [*Cheng et al.*, 1987] as none have the appropriate trace element and isotopic compositions. Sample 119-2-5 represents an adequate end-member (see Table S2 for the end-member compositions), better than Samoan islands [*Palacz and Saunders*, 1986; *Wright and White*, 1987; *Farley et al.*, 1992; *Workman et al.*, 2004; *Jackson et al.*, 2007, 2010]. Indeed, thee FSC samples less affected by the fluid-dominated subduction component plot near the mixing curve between a depleted melt (ELSC-like) and sample 119-2-5. The offset from the curve toward high $^{87}Sr/^{86}Sr$ reflects the contribution of the fluid-dominated subduction component.

physical separation of discrete volcanic edifices despite what is likely a continuous flux of subduction components from the slab. A physical mechanism to account for the volcano separation must involve 3-D flow in the mantle wedge, possibly related to convective rolls parallel to the trench. Such secondary convection could lead to regular volcano spacing. This flow pattern would extend toward the back-arc, focusing subduction components on lines perpendicular to the arc volcanic front. Such a process could be self-sustaining. The onset of vertical flow in the mantle wedge would focus subduction components coming off the slab into the upwelling region. This would lead to enhanced melting and vertical flow, providing preferred pathways for both melting and subduction components. Such upwelling could lead to linear focusing of subduction components without lateral flow at shallow levels. The existence of such a flow regime might also facilitate the "capture" of the arc by the back-arc as the back-arc gets very close to the arc, as appears to be the case for portions of this region [*Keller et al.*, 2008].

5.3. Distinguishing the Effect of Mantle Melting, Mantle Source and Subduction Input

[66] In this section, we discuss the effect of fluid addition, enriched mantle and degree of melting

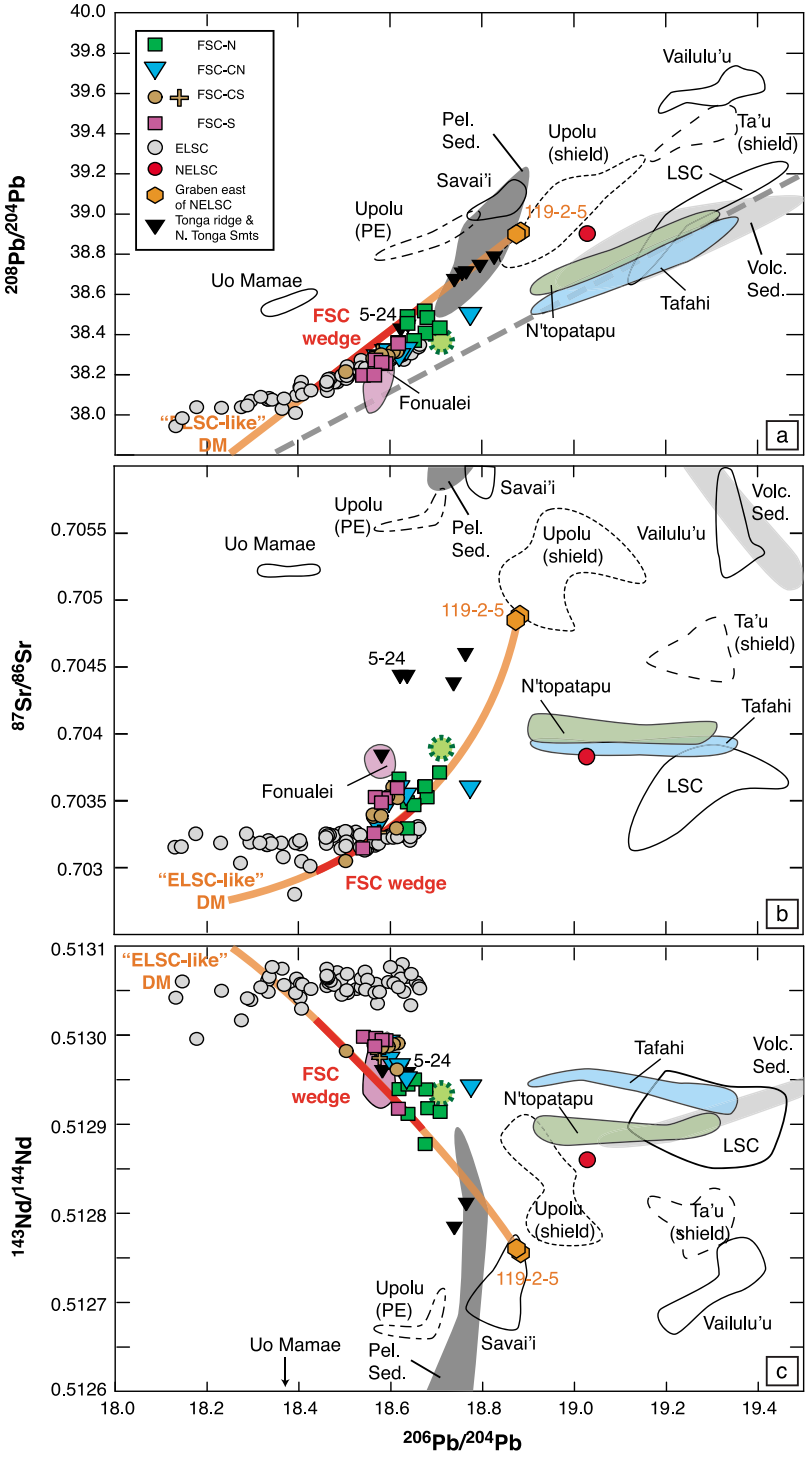
FSC-N
FSC-CN
FSC-CS
FSC-S
ELSC
NELSC
Graben east of NELSC
Tonga ridge & N. Tonga Smts
$^{208}Pb/^{204}Pb$
$^{87}Sr/^{86}Sr$
$^{143}Nd/^{144}Nd$
$^{206}Pb/^{204}Pb$
Vailulu'u
Pel. Sed.
Upolu (shield)
Ta'u (shield)
Savai'i
LSC
Upolu (PE)
119-2-5
Volc. Sed.
Uo Mamae
Tafahi
FSC wedge
5-24
N'topatapu
Fonualei
"ELSC-like" DM
a
b
c

Figure 12

using the major and trace elements for the different geographical groups. *Taylor and Martinez* [2003], *Langmuir et al.* [2006] and *Bézos et al.* [2009] have shown that the low $Ti_{8.0}$-$Na_{8.0}$-$Fe_{8.0}$ end-members of the trends defined by different back-arc spreading centers (Figure 4) have the highest $H_{8.0}$ and reflect the largest extents of integrated melting. The influence of water on extent of melting is therefore critical. While we cannot use water contents of the FSC lavas because of degassing, we can still estimate the relative amounts of water in the various lavas using ratios sensitive to the fluid addition and not significantly affected by the extent of melting (such as Ce/Pb). The tight correlations among $Na_{8.0}$, $Ti_{8.0}$ and Ce/Pb (Figure 7) confirm that the low $Na_{8.0}$, low $Ti_{8.0}$ samples are associated with the strongest subduction input illustrated by low Ce/Pb which is a first-order proxy for the amount of water present in the mantle source. Both the arc-like end-member and 119-2-5 (proxy for the enriched mantle) have low Ce/Pb ratios and represent components with high water contents, consistent with high degrees of melting. Indeed, very low $Na_{8.0}$ and $Ti_{8.0}$ (Figure 5) suggest the total amount of melting indicated by the FSC lavas is greater even than the ELSC [*Bézos et al.*, 2009] or Manus Basin [*Sinton et al.*, 2003], which were previously the highest extents of melting recorded in back-arc lavas [*Langmuir et al.*, 2006].

[67] These low abundances for the FSC as a whole could reflect melting of a more depleted source, higher extents of melting, or both. There are two lines of evidence suggesting the average source is not exceptionally depleted. The first is the high La/Sm and particularly Nb/Zr measured in the FSC lavas that require a more enriched source than the ELSC/ValuFa mantle source (Figure 9). Note this elevation is true even for the lowest Nb/Zr samples in this region (Figure 9). The high Nb/Zr is not associated with subduction components, and may indicate overall source enrichment. The second is the low and flat heavy rare earth (HREE) contents, substantially lower than Valu Fa lavas (Figure 3a). Because the HREE content of the mantle source is not very sensitive to degree of mantle depletion/enrichment, and depletion often causes relative depletion of the MREE relative to the HREE (e.g., low Sm/Yb), the low and flat HREE are most readily explained by higher extent of recent melting rather than previous source depletion. Higher extents of melting are also consistent with more fluid-mobile element enrichment (e.g., Ce/Pb and Ba/Nb) beneath the Fonualei Spreading Centers compared beneath the ELSC/ValuFa Spreading Center. Such enrichment in a subduction component is likely associated with higher water contents, which would enhance the extent of melting.

[68] There then appear to be two major effects on trace element abundances and extents of melting. The first is the regional change in mantle enrichment, and the second is the influence of the subduction component leading to varying extents of melting. The change in Nb/Zr is largely source influence. The changes in abundances of $Nb_{8.0}$ and $Zr_{8.0}$ at constant Nb/Zr reflect differences in extent of melting. These considerations permit the development of the simple quantitative model discussed below.

5.3.1. Model Description

[69] The model determines the degree of melting as well as the proportion of depleted and enriched mantle components for each sample using ratios of two non-mobile trace elements (Nb/Zr and La/Sm) and the TiO_2 contents of the lavas. A second step calculates the amount of Ba (ppm) added to the mantle source for each sample that can be used as a proxy for the amount of subduction component.

[70] The compositions of the two mantle sources are critical for our calculations and are to a certain extent arbitrary. The calculated extents of melting depend strongly on the TiO_2 contents for the mantle sources. It is the relative variations that are the most robust results. We estimate the compositions of

Figure 12. Pb-Sr-Nd isotope diagrams. The FSC samples are plotted with samples from the ELSC [*Escrig et al.*, 2009], from the northern part of the Lau Basin [*Falloon et al.*, 2007], the Tonga arc islands [*Jenner et al.*, 1987; *Turner et al.*, 1997; *Ewart et al.*, 1998; *Hergt and Woodhead*, 2007; *Pearce et al.*, 2007; *Escrig et al.*, 2009], the Samoan islands [*Palacz and Saunders*, 1986; *Wright and White*, 1987; *Farley et al.*, 1992; *Workman et al.*, 2004; *Jackson et al.*, 2007, 2010], pelagic and volcaniclastic sediments from the Site 204 [*Turner et al.*, 1997; *Ewart et al.*, 1998] and the Louisville Seamount Chain [*Cheng et al.*, 1987]. The 3 southernmost FSC segments trend toward the field of Fonualei, while the FSC-N is shifted toward higher $^{206}Pb/^{204}Pb$, reflecting both a different subduction input (intermediate between N. Tonga islands and Fonualei) and the presence of the enriched mantle component. As in Figure 11, the green filled dashed circle, intermediate between Fonualei and Tafahi, represents a good isotopic end-member for the FSC-N trend. The mixing curve (see Table S2 for the end-members' compositions) between a ELSC-like depleted mantle melt and sample 119-2-5 goes through the FSC samples with the lowest subduction input, and the other samples plot between the curve and the arc fields (representing proxies for the subduction components).

the two mantle sources by first selecting a source TiO_2 content. We pick 0.12% TiO_2 for the depleted source, slightly lower than the depleted value of 0.13% of *Salters and Stracke* [2004], and 0.165% TiO_2 for the enriched mantle source, assuming that some TiO_2 was added with the enriched component that created the source. Then, using the most enriched and most depleted lavas from the FSC and NE-LSC, we calculate the extent of melting of these samples, which is 33% and 15% for depleted and enriched sources. From these extents of melting, we can then invert the source concentrations of the other elements. Note that the depleted mantle composition ("DM" in Figures 10–12), while consistent isotopically with the most depleted samples found in the ELSC far to the south of this region, has lower Nb/Zr even than the most depleted FSC lavas. We use a less depleted end-member composition that is closer to the range of the FSC lavas, as indicated by the colored portion of the mixing curves in Figures 10–12. Table S3 contains the source compositions and partition coefficients.

[71] Our calculations were made using compositions corrected back to Fo_{90} (first by correcting each lava to the MgO content where either plagioclase and cpx first appears and then olivine addition (see *Bézos et al.* [2009] for details)). The correction to Fo_{90} does not change ratios of incompatible trace elements as their contents are calculated assuming a constant element/K_2O ratio (i.e., assuming a similar low partition coefficient as K_2O). Despite the involvement of a refractory mantle (i.e., the trace element - enriched mantle source), we prefer Fo_{90} rather than a higher value because our calculations show that the dominant mantle source remains the depleted mantle source (see results below).

[72] For each sample, for a given F, there is only one fraction of depleted mantle (X_{DM}) that can reproduce its trace element ratio (either La/Sm or Nb/Zr). The equation giving X_{DM} is derived from the combination of mass balance and batch melting equations.

[73] The mass balance equation for an element "Elt" gives

$$Elt_{source} = [X_{DM}.Elt_{DM}] + [(1 - X_{DM}).Elt_{EM}], \quad (1)$$

with X_{DM} the fraction of depleted mantle.

[74] Combining (1) with the batch melting equation

$$Elt_{melt} = \frac{Elt_{source}}{D + F.(1 - P)}, \quad (2)$$

the mass balance equation leads to

$$Elt_{melt} = \frac{X_{DM}.Elt_{DM} + (1 - X_{DM}).Elt_{EM}}{D_{Elt} + F.(1 - P_{Elt})}. \quad (3)$$

Using this equation, we can write that for every sample (here for Nb/Zr)

$$\left(\frac{Nb}{Zr}\right)_{melt} = \frac{\left(\frac{X_{DM}.Nb_{DM} + (1 - X_{DM}).Nb_{EM}}{D_{Nb} + F.(1 - P_{Nb})}\right)}{\left(\frac{X_{DM}.Zr_{DM} + (1 - X_{DM}).Zr_{EM}}{D_{Zr} + F.(1 - P_{Zr})}\right)}. \quad (4)$$

Re-arranging equation (4) to extract X_{DM} as a function of F, the source's composition and $\left(\frac{Nb}{Zr}\right)_{melt}$

$$X_{DM} = \frac{Nb_{EM}.(D_{Zr} + F.(1 - P_{Zr})) - \left(\frac{Nb}{Zr}\right)_{melt}.Zr_{EM}.(D_{Nb} + F.(1 - P_{Nb}))}{\left(\frac{Nb}{Zr}\right)_{melt}.(Zr_{DM} - Zr_{EM}).(D_{Nb} + F.(1 - P_{Nb})) - (Nb_{Dm} - Nb_{EM}).(D_{Zr} + F.(1 - P_{Zr}))}. \quad (5)$$

In order to determine F, we use the independent constraint brought by the TiO_2 content. F is optimized so that the TiO_2 content for the calculated source, which is a function of X_{DM}, gives the exact TiO_2 content for the lavas for each sample. After a starting F is picked, the fraction of depleted mantle X_{DM} needed to get a mantle source that reproduces the exact Nb/Zr (or La/Sm) ratio is calculated using equation (5). The corresponding TiO_2 content of the source is calculated using equation (1):

$$TiO2_{source} = X_{DM}.TiO2_{DM} + (1 - X_{DM}).TiO2_{EM}. \quad (6)$$

[75] Using the TiO_2 composition calculated for the source and the starting F, equation (2) does not at first reproduce the TiO_2 content of the sample, and F has to be adjusted until the calculated and measured TiO_2 contents are consistent. The method is described in detail in the spreadsheet available as auxiliary material. For each sample, the measured TiO_2 content, the calculated source and a re-arranged equation (2) applied to TiO_2,

$$F = \frac{\frac{TiO2_{source}}{TiO2_{melt}} - D_{TiO2}}{(1 - P_{TiO2})}, \quad (7)$$

are used to calculate an "output" F. This calculated F should be similar to the starting value used to calculate X_{DM}. By replacing the starting value by the calculated value a few times, the two F values

converge rapidly, reproducing both the trace element ratio and the TiO_2 content.

[76] Due to the high extent of melting and the possible exhaustion of clinopyroxene, we chose to use partition coefficients varying with the extent of melting. The details of the determination of the relationship between D and F are reported in Table S5. By increments of 1%, a starting mineralogy is melted and the mineralogy of the residual solid is calculated using melting equations. Clinopyroxene's exhaustion occurs at F $\sim$ 26.8% and othopyroxene's exhaustion at F $\sim$ 45.9%. At each step and for each element, a bulk partition coefficient is calculated. Linear regressions of D versus F (between 10% and 26% and 26.8% and 45.8%) give the equations of D as a function of F that are used in our model.

[77] Nb/Zr and La/Sm were treated separately in order to get two sets of independent results. Both ratios yield similar degree of melting (better than $\pm$1.61% of the calculated value, e.g., 12.28% and 12.09%, Figure S2) and proportions of depleted mantle (better than a few % of the calculated value, e.g., 99.47% and 96.18%). The proportions of X_{DM} are almost always lower for the La/Sm calculations, probably because some La is contributed by the subduction component. The relative variation in mantle fractions between the samples is the key result.

[78] It is worth noting that, despite the fact that our optimization is only based on *trace element ratios* and *TiO_2 content*, our results reproduce very well the Nb, Zr, La and Sm *contents* of the lavas (see Figure S5). The good agreement between the measured and calculated trace element contents confirm the validity of our approach and the good approximation for the depleted and enriched mantle sources.

[79] The second step of the model estimates the contribution of the subduction input. As we have calculated the Nb content for the source of each sample, we use the Ba/Nb ratio of normal (Ba/Nb $\sim$ 2) and enriched (Ba/Nb $\sim$ 6) MORB far from subduction zones to calculate the background Ba content of the two mantle source end-members prior to the addition of the subduction component. Inverting the effect of melting using the F calculated during the first step, we then calculate for each sample the Ba content of its source, The additional Ba above the background mantle (calculated using the proportions from the first step) is the contribution of the subduction component.

5.3.2. Model Results

[80] Our model shows that the degree of melting ranges from 20% to 25% in the 3 southern FSC groups except for the boninitic samples where there are larger extents of melting, up to 38% (Figure 13). The FSC-N requires lower degree of melting, but still greater than 9%. The degree of melting does not correlate with the fraction of enriched mantle (Figure 13d) confirming that the extent of melting beneath the spreading center is not controlled to first order by mantle fertility. The degree of melting within the FSC alone also does not correlate with the slab depth (Figure 14c), a conclusion also reached by *Keller et al.* [2008], although the northernmost samples, most distant form the arc, have the lowest extents of melting. There is, however, a correlation with the amount of Ba coming from the subduction input (Ba_{Sub}, Figure 13b), confirming the important effect of the fluid on mantle melting. Significant variation in extent of melting can be observed at a given Ba_{Sub}, even within a single group, suggesting that there may be other parameters involved or that there may be a significant variation in the composition of the subduction input (e.g., Ba/H_2O). Overall, the correlation observed within each group (especially FSC-S and FSC-N) supports that Ba_{Sub} is a good proxy for the amount of subduction input.

[81] The fraction of enriched mantle displays some interesting variation with latitude (Figure 13c). It increases slightly but regularly toward the north within the FSC-S, drops at the FSC-S/FSC-CS boundary, and increases in the 3 northern groups (Figure 13c). Given the uncertainties, it may be roughly constant in the south, and then increase north of 17°S, as also indicated by the Nd isotopes.

[82] There is a small contrast between the boninitic samples from the FSC-CS and -CN. Both groups have a similar range of extent of melting while the FSC-CN has a higher fraction of enriched mantle and a higher contribution of subduction input (Figure 13). A greater contrast occurs for the FSC-N and FSC-S. For samples with similar Ba_{Sub} (i.e., a similar amount of subuction input), the extent of melting is lower for the FSC-N, where there is a much higher proportion of enriched (but refractory) mantle (Figure 13b). Assuming that the addition of the subduction input enhances melting, this would be consistent with the enriched mantle component being refractory, as proposed by *Falloon et al.* [2007] for the source of 119-2-5 that represents the enriched mantle component for the FSC.

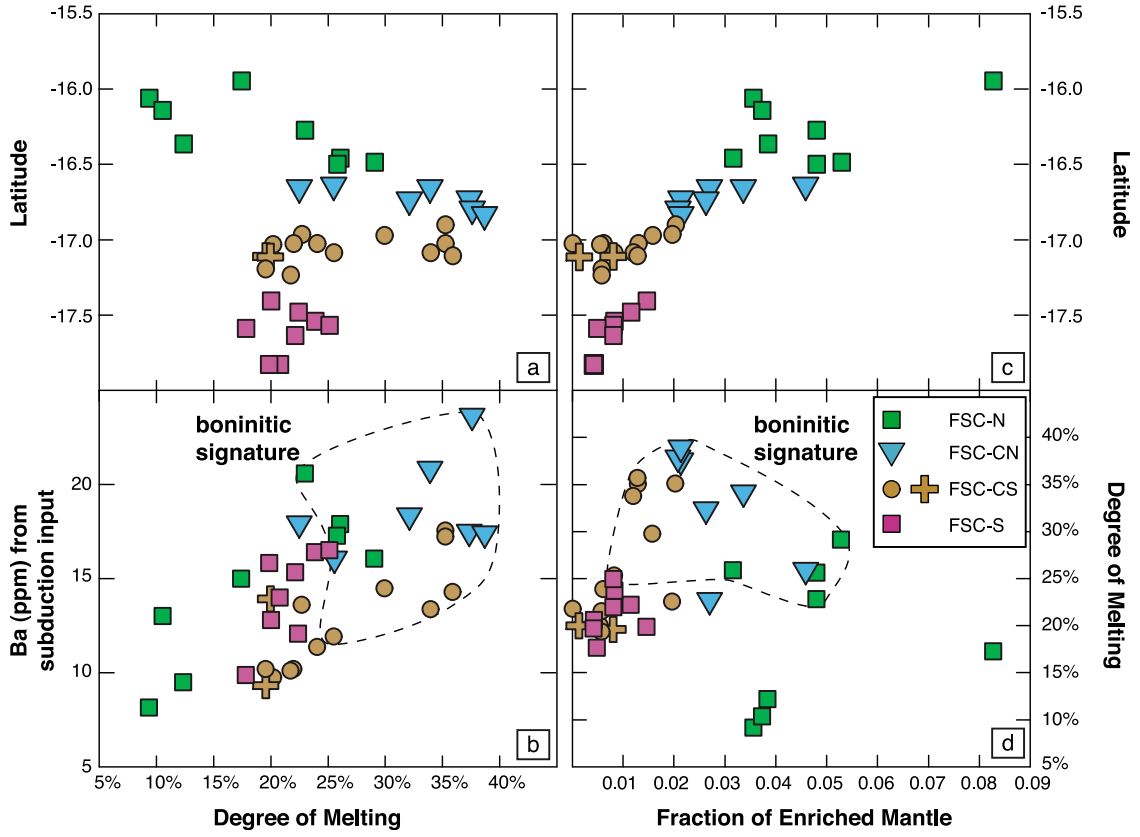

Figure 13. (a, c) Panels show the calculated variations in extent of melting and fraction of enriched mantle with latitude. (b) Panel shows the extent of melting correlates with the subduction input, using the amount of Ba (ppm) added to the source as a proxy for the subduction input. (d) Panel shows the lack of correlation between extent of melting and fraction of enriched mantle. Samples with a boninitic signature are all localized between 16.2°S and 17.1°S and correspond to the highest extents of melting in the area. The boninitic samples have higher extents of melting compared to the other samples with similar Ba input from the subduction component, suggesting possibly a higher H_2O/Ba ratio in the subduction component.

5.4. Origin of the Boninitic Samples

[83] Our data and model show that the boninitic signature, localized between 16.2°S and 17.1°S, is associated with the highest degree of melting, an important fluid component and a refractory mantle component (Figure 13). These results are consistent with the model proposed by *Danyushevsky et al.* [1995] and later *Falloon et al.* [2007] for the boninites found in the Northern Lau Basin, requiring the combination of a refractory mantle, an OIB-derived melt component.

[84] In the northern Lau Basin, the presence of boninitc samples in a back-arc environment is related to abnormal behavior of the adjoining arc volcanism. The location of the boninitic samples corresponds to the area where the submarine arc volcanoes seem to be inactive, and to a local increase in mobile elements leading to Ba_{Sub} comparable to what is otherwise observed much closer to the arc front. As proposed by *Keller et al.* [2008], it appears that subduction flux normally delivered to the volcanic front is drained toward the back-arc spreading center and is responsible for arc-like compositions.

[85] Further south in the Lau Basin, *Cooper et al.* [2010] also proposed high degrees of melting of a refractory mantle source for the origin of boninites. This is consistent with what we observe, but the general model they propose for boninitic magmatism does not apply. They propose that the refractory mantle is produced by back-arc melting, and this mantle is subsequently supplied to the arc by lateral flow. The subduction flux then causes melting of the refractory mantle produced by melting at the back-arc. In the FSC, the boninitic heritage occurs in the back-arc, not the arc. A general model for producing boninites seems to require a depleted mantle and water-rich flux. As observed in the Lau Basin,

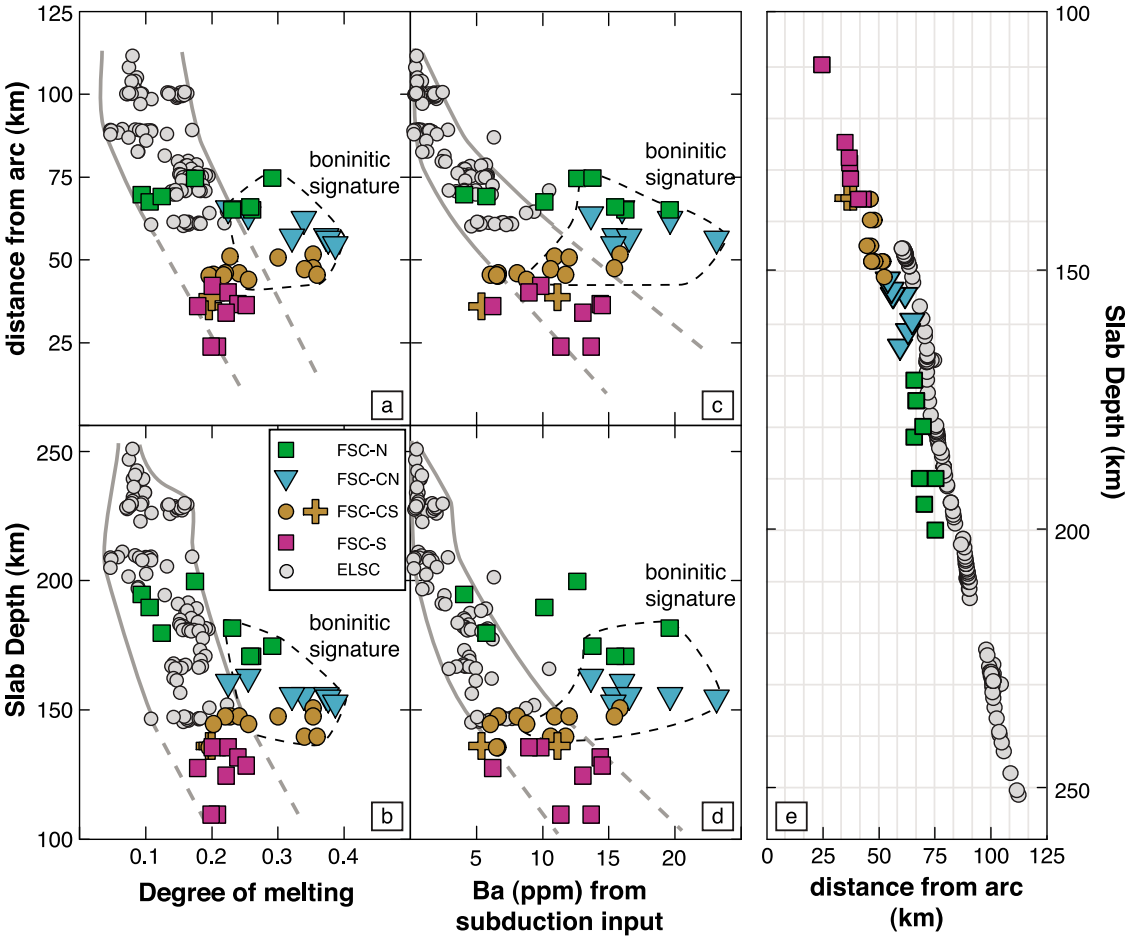

Figure 14. (a–d) Variation of the degree of melting and the Ba contribution from the subduction input with the slab depth and the distance from the arc for the FSC and ELSC and (e) slab depth versus distance from the arc. The slab depth for the ELSC is extracted from the USGS grid (http://earthquake.usgs.gov/research/data/slab/) and for the FSC is from *Keller et al.* [2008]. The extents of melting for the ELSC samples [*Bézos et al.*, 2009; unpublished data] are calculated following *Bézos et al.*'s [2009] approach (trace element data corrected to Fo90), assuming a source with constant Lu (Lu_0 = 0.056 ppm). The Ba of the source for each sample is then calculated and the contribution of the Ba from the subduction input is deduced using Ba/Nb ~ 2 for the source. The FSC-S and the non-boninitic samples extend the ELSC trend, while the boninites are offset toward higher degree of melting and Ba input at a given slab depth and distance from the arc.

there are several tectonic settings where that can occur.

[86] There is the question of why the back-arc would capture the subduction component in some cases but not others. The numerical models of *Harmon and Blackman* [2010] suggest that close to the arc, the melting regimes beneath the arc and back-arc are connected. This particular numerical model does not however explain the absence of melt supply to the arc volcanoes when the back-arc is slightly further away, nor the clear separation of arc and back-arc in the southern Lau Basin (i.e., Valu Fa and Ata) even when the two have small separation.

5.5. Comparison of the FSC and ELSC

[87] The comparison of physical parameters such as the slab depth and distance from the arc with the geochemical data provide interesting insights on the processes occurring beneath the Fonualei Spreading Center and the Eastern Lau Spreading Center.

[88] The location of the earthquake epicenters reveal that the slab subducting beneath the ELSC goes down with a steeper angle than below the FSC. Also, for the FSC, the distance from the arc increases northward twice as fast as for the ELSC. The combination of both parameters is illustrated in Figure 14e.

[89] Variation of degree of melting with slab depth and distance from the arc shows three very important features (for the ESLC, we used the method described in *Bézos et al.* [2009], see caption for details). 1- the ELSC defines a trend with an increase of the degree of melting toward the arc as slab depth decreases; 2- most of the FSC non-boninitic samples extend the ELSC trend while the boninites are offset toward higher melting values; 3- the boninites are offset toward higher Ba_{Sub} relative to the ELSC trend for a comparable distance from the arc and slab depth. It is this character that also produces a lack of clear correlation between slab depth and extent of melting for the FSC alone.

[90] For the ELSC, the distance from the arc and the slab depth both increase toward the north. There is no evidence for significant changes in major and trace element contents of the depleted mantle wedge beneath the ELSC. And, although the character of the subduction input does vary [see *Escrig et al.*, 2009], the amount of subduction component in the ELSC generally decreases with the distance from the arc, with a corresponding effect on the extent of melting. A decrease in subduction input (Ba_{Sub}) causes a decrease in extent of melting with the distance from the arc and thus with an increasing slab depth.

[91] The second feature is quite surprising as the FSC and ELSC differ significantly in the geometry of the subduction zone (slab angle, convergence rate, angle between the spreading center and the arc front). The fast convergence rate of the subducting plate near the FSC is expected to lead to higher extents of melting because the faster subduction advects the mantle more rapidly into the wedge corner, leading to higher mantle temperatures. The FSC-S, however, extends the ELSC trends, suggesting that convergence rate is not playing a significant role. A clear discontinuity between the FSC-S and the other FSC groups is apparent in the latitudinal plots (Figure 8 and 13c). The FSC-S lavas do not have a boninitic signature as seen a few kilometers north. The FSC-S is located nearby Fonualei Island. The high Ba_{Sub} of the FSC-S lavas relative to the ELSC can simply be explained by its being closer to the arc.

[92] The third major feature (i.e., the offset from the ELSC trend of the boninitic samples in Figure 14) is related to the capture of the arc component by the back-arc. Indeed, in Figures 14a and 14c, for the boninitic heritage samples, the Ba flux appears to be at the level that would be expected from a zero distance to the arc front. This contrasts with the FSC-S, where there is an active arc volcano in front of the back-arc. The higher flux relative to the ELSC is also observed in part of FSC-N, where the volcanic front is still inactive. But in this case, the FSC is sufficiently far behind the (extinct) volcanic front that it does not receive the full subduction flux.

6. Conclusions

[93] New major element, trace element and isotope data reveal a multitude of interesting features allowing the characterization of the processes affecting the source of the Fonualei Spreading Center lavas.

[94] The major element data reveal the presence of a boninitic heritage in some of the FSC samples in a limited geographical area. The trace element data show that these boninitic samples present relatively high enrichment in fluid-mobile elements, comparable to what is observed closer to the arc front.

[95] The trace element and isotope data confirm the presence of an enriched (OIB-like) mantle in the area. The enrichment is particularly evident when comparing the FSC and the other Lau spreading centers located further south in the Lau Basin (e.g., Valu Fa or ELSC). The enriched mantle component appears to be a refractory mantle enriched in trace elements by a low-F melt, similar to the source of the *Intermediate* boninitic end-member identified by *Falloon et al.* [2007] in the lavas located in the NE corner of the Lau Basin. Our quantitative modeling shows an increasing proportion of the enriched mantle component toward the north, consistent with the inferences of *Keller et al.* [2008]. We propose that the enriched mantle component is derived from a refractory plume material crossing the Vitiaz transform, where it has been slightly influenced by a subduction component in order to explain its slight enrichment in mobile elements.

[96] Our new geochemical data and the latitudinal variation show a coupling between the back-arc and the adjacent arc volcanism, confirming what had been proposed for the southern ELSC [*Escrig et al.*, 2009]. When the back-arc is close to the arc front, the arc and back-arc lavas require similar "flavors" of subduction inputs. Moreover, the locations of spikes in subduction input along the FSC correspond to the locations of the volcanoes along the arc front. This is important because most of the underwater volcanoes along the Tonga volcanic front appear to be inactive which requires that the subduction input is currently focused beneath the back-arc spreading center [*Keller et al.*, 2008].

Further away from the arc front, the correspondence between the peaks in subduction input along the spreading center and the arc volcano locations seems robust, but the geochemical relationship needs to be tested with further data from Tonga submarine arc volcanoes.

[97] Quantitative modeling of the trace element data (degree of melting, proportion of enriched mantle in the background mantle and amount of subduction input) reveal that the extent of melting is controlled by the proportion of refractory (trace element-enriched) mantle, the amount of subduction input and the mantle wedge temperature. The FSC-S behaves similarly to the ELSC, with higher extents of melting associated with a greater subduction flux and being closer to the arc. The boninitic samples found in the center of the FSC reflect the combination of a higher proportion of refractory mantle and larger amounts of the fluid-dominated component, apparently captured from the volcanic front, leading to particularly high extents of melting (up to 38%).

[98] The location of the boninites is likely related to the fact that the nearby arc volcanoes are inactive and most of the subduction input is drawn in by the melting regime beneath the spreading center. In the northernmost group (FSC-N), higher proportions of refractory mantle lessen the effect of high amounts of the fluid-dominated component (comparable to the boninitic samples) and lavas display lower extent of melting. The Fonualei Spreading Centers illustrate the complexity in interpreting data from a back-arc basin, and the importance of both subduction input and background mantle in producing back-arc magmas. Boninites occur where there is the juxtaposition of a high subduction input and a refractory mantle, an occurrence that can be produced by multiple causes.

Acknowledgments

[99] We thank Jurek Blusztajn for his assistance and support with isotope analyses at WHOI, the reviewers K. Kelley, M. Regelous and S. Turner and the associate editor D. Peate for their comments that helped to improve the manuscript. This work was supported by the National Science Foundation (OCE-0751844).

References

Asimow, P. D., and C. H. Langmuir (2003), The importance of water to oceanic mantle melting regimes, *Nature*, *421*(6925), 815–820, doi:10.1038/nature01429.

Bézos, A., S. Escrig, C. H. Langmuir, P. J. Michael, and P. D. Asimow (2009), Origins of chemical diversity of back-arc basin basalts: A segment-scale study of the Northern Eastern Lau Spreading Center, *J. Geophys. Res.*, *114*, B06212, doi:10.1029/2008JB005924.

Cheng, Q., K.-H. Park, J. D. MacDougall, A. Zindler, G. W. Lugmair, H. Staudigel, J. Hawkins, and P. Lonsdale (1987), Isotopic evidence for a hotspot origin of the Louisville Seamount Chain, in *Seamounts, Islands, and Atolls*, *Geophys. Monogr. Ser.*, vol. 43, edited by B. H. Keating et al., pp. 283–296, AGU, Washington, D. C., doi:10.1029/GM043p0283.

Cooper, L. B., T. Plank, R. J. Arculus, E. H. Hauri, P. S. Hall, and S. W. Parman (2010), High-Ca boninites from the active Tonga Arc, *J. Geophys. Res.*, *115*, B10206, doi:10.1029/2009JB006367.

Crawford, A. J., T. J. Falloon, and D. H. Green (1989), Classification, petrology, geochemistry and tectonic settings of boninites, in *Boninites and Related Rocks*, edited by A. J. Crawford, pp. 1–49, Unwin Hyman, London.

Danyushevsky, L. V. (2001), The effect of small amounts of H_2O on crystallisation of mid-ocean ridge and backarc basin magmas, *J. Volcanol. Geotherm. Res.*, *110*(3–4), 265–280, doi:10.1016/S0377-0273(01)00213-X.

Danyushevsky, L. V., A. V. Sobolev, and T. J. Falloon (1995), North Tongan high-Ca boninite petrogenesis: The role of Samoan plume and subduction zone-transform fault transition, *J. Geodyn.*, *20*(3), 219–241, doi:10.1016/0264-3707(95)00013-Y.

Dixon, J. E., E. Stolper, and J. R. Delaney (1988), Infrared spectroscopic measurements of CO_2 and H_2O in Juan de Fuca Ridge basaltic glasses, *Earth Planet. Sci. Lett.*, *90*, 87–104, doi:10.1016/0012-821X(88)90114-8.

Dixon, J. E., E. M. Stolper, and J. R. Holloway (1995), An experimental study of water and carbon dioxide solubilities in mid ocean ridge basaltic liquids. 1. Calibration and solubility models, *J. Petrol.*, *36*(6), 1607–1631.

Escrig, S., A. Bézos, S. L. Goldstein, C. H. Langmuir, and P. J. Michael (2009), Mantle source variations beneath the Eastern Lau Spreading Center and the nature of subduction components in the Lau basin-Tonga arc system, *Geochem. Geophys. Geosyst.*, *10*, Q04014, doi:10.1029/2008GC002281.

Ewart, A., K. D. Collerson, M. Regelous, J. I. Wendt, and Y. Niu (1998), Geochemical evolution within the Tonga-Kermadec Lau arc back-arc systems: The role of varying mantle wedge composition in space and time, *J. Petrol.*, *39*(3), 331–368, doi:10.1093/petroj/39.3.331.

Falloon, T. J., and A. J. Crawford (1991), The petrogenesis of high-calcium boninite lavas dredged from the northern Tonga ridge, *Earth Planet. Sci. Lett.*, *102*, 375–394, doi:10.1016/0012-821X(91)90030-L.

Falloon, T. J., A. Malahoff, L. P. Zonenshain, and Y. Bogdanov (1992), Petrology and geochemistry of back-arc basin basalts from Lau Basin spreading ridges at 15, 18, and 19°S, *Mineral. Petrol.*, *47*, 1–35, doi:10.1007/BF01165295.

Falloon, T. J., L. V. Danyushevsky, T. J. Crawford, R. Maas, J. D. Woodhead, S. M. Eggins, S. H. Bloomer, D. J. Wright, S. K. Zlobin, and A. R. Stacey (2007), Multiple mantle plume components involved in the petrogenesis of subduction-related lavas from the northern termination of the Tonga Arc and northern Lau Basin: Evidence from the geochemistry of arc and backarc submarine volcanics, *Geochem. Geophys. Geosyst.*, *8*, Q09003, doi:10.1029/2007GC001619.

Falloon, T. J., L. V. Danyushevsky, A. J. Crawford, S. Meffre, J. D. Woodhead, and S. H. Bloomer (2008), Boninites and adakites from the northern termination of the tonga trench:

Implications for adakite petrogenesis, *J. Petrol.*, *49*(4), 697–715, doi:10.1093/petrology/egm080.

Farley, K., J. Natland, and H. Craig (1992), Binary mixing of enriched and undegassed (primitive?) mantle components (He, Sr, Nd, Pb) in Samoan lavas, *Earth Planet. Sci. Lett.*, *111*, 183–199, doi:10.1016/0012-821X(92)90178-X.

Harmon, N., and D. K. Blackman (2010), Effects of plate boundary geometry and kinematics on mantle melting beneath the back-arc spreading centers along the Lau Basin, *Earth Planet. Sci. Lett.*, *298*, 334–346, doi:10.1016/j.epsl.2010.08.004.

Hawkins, J. W. (1995), The geology of the Lau Basin, in *Back-arc Basin: Tectonics and Magmatism*, edited by B. Taylor, pp. 63–138, Plenum, New York.

Hergt, J. M., and J. D. Woodhead (2007), A critical evaluation of recent models for Lau-Tonga arc-backarc basin magmatic evolution, *Chem. Geol.*, *245*, 9–44, doi:10.1016/j.chemgeo.2007.07.022.

Hofmann, A. W., K. P. Jochum, H. M. Seufert, and W. M. White (1986), Nb and Pb in oceanic basalts: New constraints on mantle evolution, *Earth Planet. Sci. Lett.*, *79*, 33–45, doi:10.1016/0012-821X(86)90038-5.

Jackson, M. G., S. R. Hart, A. A. P. Koppers, H. Staudigel, J. Konter, J. Blusztajn, M. Kurz, and J. A. Russell (2007), The return of subducted continental crust in Samoan lavas, *Nature*, *448*(7154), 684–687, doi:10.1038/nature06048.

Jackson, M. G., S. R. Hart, J. G. Konter, A. A. P. Koppers, H. Staudigel, M. D. Kurz, J. Blusztajn, and J. M. Sinton (2010), Samoan hot spot track on a "hot spot highway": Implications for mantle plumes and a deep Samoan mantle source, *Geochem. Geophys. Geosyst.*, *11*, Q12009, doi:10.1029/2010GC003232.

Jenner, G. A., P. A. Cawood, M. Rautenschlein, and W. M. White (1987), Composition of back-arc basin volcanics, Valu Fa ridge, Lau basin: Evidence foe a slab-derived component in their mantle source, *J. Volcanol. Geotherm. Res.*, *32*, 209–222, doi:10.1016/0377-0273(87)90045-X.

Keller, N. S., R. J. Arculus, J. Hermann, and S. Richards (2008), Submarine back-arc lava with arc signature: Fonualei Spreading Center, northeast Lau Basin, Tonga, *J. Geophys. Res.*, *113*, B08S07, doi:10.1029/2007JB005451.

Klein, E. M., and C. H. Langmuir (1987), Global correlations of ocean ridge basalt chemistry with axial depth and crustal thickness, *J. Geophys. Res.*, *92*, 8089–8115, doi:10.1029/JB092iB08p08089.

Langmuir, C. H., A. Bézos, S. Escrig, and S. W. Parman (2006), Chemical systematics and hydrous melting of the mantle in back-arc basins, in *Back-Arc Spreading Systems: Geological, Biological, Chemical, and Physical Interactions*, *Geophys. Monogr. Ser.*, vol. 166, edited by D. M. Christie et al., pp. 87–146, AGU, Washington, D. C., doi:10.1029/166GM07.

Lupton, J. E., R. J. Arculus, R. R. Greene, L. J. Evans, and C. I. Goddard (2009), Helium isotope variations in seafloor basalts from the Northwest Lau Backarc Basin: Mapping the influence of the Samoan hotspot, *Geophys. Res. Lett.*, *36*, L17313, doi:10.1029/2009GL039468.

McDonough, W. F., and S. S. Sun (1995), The composition of the Earth, *Chem. Geol.*, *120*, 223–253, doi:10.1016/0009-2541(94)00140-4.

Michael, P. (1995), Regionally distinctive sources of depleted MORB: Evidence from trace elements and H_2O, *Earth Planet. Sci. Lett.*, *131*(3–4), 301–320, doi:10.1016/0012-821X(95)00023-6.

Michael, P. J., and R. L. Chase (1987), The influence of primary magma composition, H_2O and pressure on midocean ridge basalt differentiation, *Contrib. Mineral. Petrol.*, *96*(2), 245–263, doi:10.1007/BF00375237.

Palacz, Z. A., and A. D. Saunders (1986), Coupled trace element and isotope enrichment in the Cook-Austral-Samoa Island, Southern Pacific, *Earth Planet. Sci. Lett.*, *79*, 270–280, doi:10.1016/0012-821X(86)90185-8.

Pearce, J. A., M. Ernewein, S. H. Bloomer, L. M. Parson, B. J. Murton, and L. E. Johnson (1994), Geochemistry of Lau Basin volcanic rocks: Influence of ridge sementation and arc proximity, *Geol. Soc. Spec. Publ.*, *81*, 53–75, doi:10.1144/GSL.SP.1994.081.01.04.

Pearce, J. A., P. D. Kempton, and J. B. Gill (2007), Hf-Nd evidence for the origin and distribution of mantle domains in the SW Pacific, *Earth Planet. Sci. Lett.*, *260*, 98–114, doi:10.1016/j.epsl.2007.05.023.

Peate, D. W., T. F. Kokfelt, C. J. Hawkesworth, P. W. Van Calsteren, J. M. Hergt, and J. A. Pearce (2001), U-series isotope data on Lau Basin glasses: The role of subduction-related fluids during melt generation in back-arc basins, *J. Petrol.*, *42*(8), 1449–1470, doi:10.1093/petrology/42.8.1449.

Regelous, M., K. D. Collerson, A. Ewart, and J. I. Wendt (1997), Trace element transport rates in subduction zones: Evidence from Th, Sr and Pb isotope data for Tonga-Kermadec arc lavas, *Earth Planet. Sci. Lett.*, *150*, 291–302, doi:10.1016/S0012-821X(97)00107-6.

Regelous, M., S. Turner, T. J. Falloon, P. Taylor, J. Gamble, and T. Green (2008), Mantle dynamics and mantle melting beneath Niuafo'ou Island and the northern Lau back-arc basin, *Contrib. Mineral. Petrol.*, *156*(1), 103–118, doi:10.1007/s00410-007-0276-7.

Regelous, M., J. A. Gamble, and S. P. Turner (2010), Mechanism and timing of Pb transport from subducted oceanic crust and sediment to the mantle source of arc lavas, *Chem. Geol.*, *273*, 46–54, doi:10.1016/j.chemgeo.2010.02.011.

Ruellan, E., J. Delteil, I. Wright, and T. Matsumoto (2003), From rifting to active spreading in the Lau Basin–Havre Trough backarc system (SW Pacific): Locking/unlocking induced by seamount chain subduction, *Geochem. Geophys. Geosyst.*, *4*(5), 8909, doi:10.1029/2001GC000261.

Salters, V. J. M., and A. Stracke (2004), Composition of the depleted mantle, *Geochem. Geophys. Geosyst.*, *5*, Q05B07, doi:10.1029/2003GC000597.

Sinton, J. M., and P. Fryer (1987), Mariana Trough lavas from 18°N: Implications for the origin of back arc basin basalts, *J. Geophys. Res.*, *92*(B12), 12,782–12,802, doi:10.1029/JB092iB12p12782.

Sinton, J. M., L. L. Ford, B. Chappell, and M. T. McCulloch (2003), Magma genesis and mantle heterogeneity in the Manus back-arc basin, Papua New Guinea, *J. Petrol.*, *44*(1), 159–195, doi:10.1093/petrology/44.1.159.

Stolper, E. (1982), The speciation of water in silicate melts, *Geochim. Cosmochim. Acta*, *46*(12), 2609–2620, doi:10.1016/0016-7037(82)90381-7.

Tanaka, T., et al. (2000), JNdi-1: A neodymium isotopic reference in consistency with LaJolla neodymium, *Chem. Geol.*, *168*, 279–281, doi:10.1016/S0009-2541(00)00198-4.

Taylor, B., and F. Martinez (2003), Back-arc basin basalt systematics, *Earth Planet. Sci. Lett.*, *210*(3–4), 481–497, doi:10.1016/S0012-821X(03)00167-5.

Tian, L., P. R. Castillo, D. R. Hilton, J. W. Hawkins, B. B. Hanan, and A. J. Pietruszka (2011), Major and trace element and Sr-Nd isotope signatures of the northern Lau Basin lavas: Implications for the composition and dynamics of the back-

arc basin mantle, *J. Geophys. Res.*, *116*, B11201, doi:10.1029/2011JB008791.

Todt, W., R. A. Cliff, A. Hanser, and A. W. Hofmann (1996), Evaluation of a ^{202}Pb–^{205}Pb double spike for high-precision lead isotope analysis, in *Earth Processes: Reading the Isotopic Code*, *Geophys. Monogr. Ser.*, vol. 95, edited by A. Basu and S. Hart, pp. 429–437, AGU, Washington, D. C., doi:10.1029/GM095p0429.

Turner, S. P., and C. J. Hawkesworth (1997), Constraints on flux rates and mantle dynamics beneath island arcs from Tonga-Kermadec lava geochemistry, *Nature*, *389*(6651), 568–573, doi:10.1038/39257.

Turner, S. P., and C. J. Hawkesworth (1998), Using geochemistry to map mantle flow beneath the Lau Basin, *Geology*, *26*(11), 1019–1022, doi:10.1130/0091-7613(1998)026<1019:UGTMMF>2.3.CO;2.

Turner, S., C. J. Hawkesworth, N. Rogers, J. Bartlett, T. Worthington, J. M. Hergt, J. A. Pearce, and I. Smith (1997), ^{238}U-^{230}Th disequilibria, magma petrogenesis, and flux rates beneath the depleted Tonga-Kermadec island arc, *Geochim. Cosmochim. Acta*, *61*(22), 4855–4884, doi:10.1016/S0016-7037(97)00281-0.

Turner, S., J. Caulfield, T. Rushmer, M. Turner, S. Cronin, I. Smith, and H. Handley (2012), Magma evolution in the primitive, intra-oceanic Tonga Arc: Rapid petrogenesis of dacites at Fonualei Volcano, *J. Petrol.*, *53*(6), 1231–1253, doi:10.1093/petrology/egs005.

Wendt, J. I., M. Regelous, K. D. Collerson, and A. Ewart (1997), Evidence for a contribution from two mantle plumes to island-arc lavas from northern Tonga, *Geology*, *25*, 611–614, doi:10.1130/0091-7613(1997)025<0611:EFACFT>2.3.CO;2.

Workman, R. K., S. R. Hart, M. Jackson, M. Regelous, J. Blusztajn, M. Kurz, K. A. Farley, and H. Staudigel (2004), Recycled metasomatized lithosphere as the origin of the enriched mantle II (EM2) end-member: Evidence from the Samoan volcanic chain, *Geochem. Geophys. Geosyst.*, *5*, Q04008, doi:10.1029/2003GC000623.

Wright, E., and W. M. White (1987), The origin of Samoa: New evidence from Sr, Nd, and Pb isotopes, *Earth Planet. Sci. Lett.*, *81*, 151–162, doi:10.1016/0012-821X(87)90152-X.

Zellmer, K., and B. Taylor (2001), A three-plate kinematic model for Lau Basin opening, *Geochem. Geophys. Geosyst.*, *2*(5), 1020, doi:10.1029/2000GC000106.